UCRL-LR-124742

Synthesis, Electronic and Optical Properties of Si Nanostructures

Long Ngoc Dinh
(Ph.D. Thesis)

September 1996

Work performed under the auspices of the U.S. Department of Energy by Lawrence Livermore National Laboratory under Contract W-7405-ENG-48.

UCRL-LR-124742
Distribution Category UC-404

Synthesis, Electronic and Optical Properties of Si Nanostructures

Long Ngoc Dinh
(Ph.D. Thesis)

September 1996

LAWRENCE LIVERMORE NATIONAL LABORATORY
University of California • Livermore, California • 94551

Synthesis, electronic and optical properties of Si nanostructures

By

LONG NGOC DINH
B.A. (University of California, Berkeley) 1990
M.S. (University of California, Davis) 1992

DISSERTATION

Submitted in partial satisfaction of the requirements for the degree of

DOCTOR OF PHILOSOPHY

in

Engineering - Applied Science

in the

GRADUATE DIVISION

of the

UNIVERSITY OF CALIFORNIA

DAVIS

Approved:

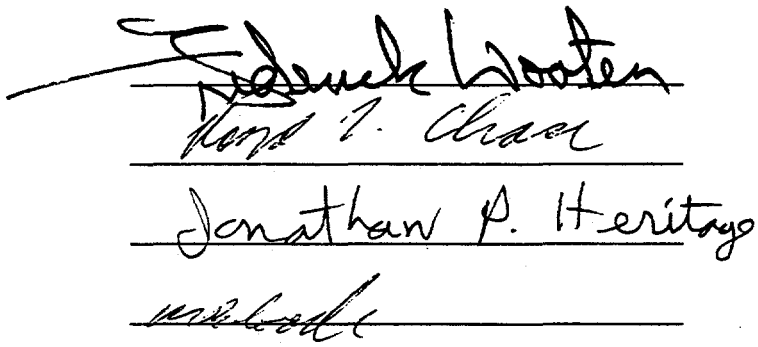

Committee in charge

1996

Abstract

Silicon and silicon oxide nanostructures have been deposited on solid substrates, in an ultra high vacuum (UHV) chamber, by laser ablation or thermal vaporization. Laser ablation followed by substrate post annealing produced Si clusters with average size of a few nanometers, on highly oriented pyrolytic graphite (HOPG) surfaces. This technique, which is based on surface diffusion, is limited to the production of less than one layer of clusters on a given surface. The low coverage of Si clusters and the possibility of nonradiative decay of excitation in the Si cores to the HOPG substrates in these samples rendered them unsuitable for many optical measurements. Multiple shot laser ablation in an Ar buffer gas produced multilayer coverage of Si clusters. Nevertheless, the size distribution of the clusters obtained from this technique was very broad, ranging from a few nanometers to many micrometers. Such wide size distributions made it difficult to systematically investigate the effect of size on the electronic and optical properties of the clusters. Thermal vaporization of Si in an Ar buffer gas, on the contrary, yielded multilayer coverage of Si nanoclusters with a fairly narrow size distribution of about 2 nm, full width at half maximum (FWHM). As a result, further study was performed only on Si nanoclusters synthesized by thermal vaporization in a buffer gas. High resolution transmission electron microscopy (HRTEM) and x-ray diffraction (XRD) revealed that these nanoclusters were crystalline. However,

during synthesis, if oxygen was the buffer gas, a network of amorphous Si oxide nanostructures (an-SiO_x) with occasional embedded Si dots was formed. All samples showed strong infrared and/or visible photoluminescence (PL) with varying decay times from nanoseconds to microseconds depending on synthesis conditions. The threshold absorption energy for the Si 2p core level, measured by x-ray absorption spectroscopy (XAS), increased as the average size of nc-Si decreased. Visible and ultraviolet absorption in the Si cores for surface passivated Si nanocrystals (nc-Si), but mainly in oxygen related defect centers for an-SiO_x, was observed by photoluminescence excitation (PLE) spectroscopy. The visible components of the PL spectra were noted to blue shift and broaden as the size of the nc-Si was reduced. There were differences in PL spectra for hydrogen and oxygen passivated nc-Si, while many common PL properties between oxygen passivated nc-Si and an-SiO_x were observed. The observed experimental results can be best explained by a model involving absorption between quantum confined states in the Si cores and emission for which the decay times are very sensitive to surface and/or interface states. The emission could involve a simple band to band recombination mechanism within the Si cores. The combined evidence of all of experimental results suggests, however, that emission between surface or interface states is a more likely mechanism.

Acknowledgment

Thank you, God, for creating me and for making this thesis possible. I would also like to thank my parents for their steady encouragement during the course of my thesis.

A lot of thanks go to Prof. Fred Wooten, my thesis advisor, who has introduced me to the field of solid state physics, and continually provided me with the intellectual support I needed in this endeavor. Significant credit for the work presented here belongs to Dr. Lloyd Chase, my research supervisor. Without his patient support, knowledgeable guidance, and understanding, this thesis could not be completed. Special thanks must go to Dr. Mehdi Balooch, who has trained me in the vacuum and surface science technology. His expertise, almost daily help, advice and care have eased my graduate student life a lot.

Professional discussions and assistance from Dr. Wigbert Siekhaus, Dr. Margaret Olsen, Dr. Alex Hamza, Dr. Louis Terminello, Dr. Troy Barbee, Dr. Carlos Colmenares, Dr. Tony Van Buuren, and Dr. John Elmer are greatly appreciated. The technical support from Barry Olsen, Randy Hill, Jim Yoshiyama, Eric Fought, Allen Witse, Dan Gnade, Wayne Thomas, Bob Smith and specially Cherryl Evans are gratefully acknowledged. Administrative assistance from Donna Baker, Sherry Christensen, Karen Sitzberger, Archietta Johson, Estelle

Miller, Donna Clifford, and Lisa Swayne are cheerfully recognized. The thoughtful advice, care and academic support from Prof. Ann Orel will definitely be remembered.

Finally, the financial support in the form of student employee fellowship from the Department of Applied Science, University of California at Davis and the Lawrence Livermore National Laboratory is also thankfully acknowledged.

Tables of Contents

List of Tables

List of Figures

List of acronyms

AFM	atomic force microscopy
an-SiO_X	amorphous silicon oxide nanostructures
a. u.	arbitrary units
AES	Auger electron spectroscopy
c-Si	crystalline silicon
EDS	electronic density of states
ELDS	electronic local density of states
FWHM	full width at half maximum
HOPG	highly oriented pyrolytic graphite
HRTEM	high resolution transmission electron microscopy
nc-Si	silicon nanocrystals
NBOHC	non bridging oxygen hole center
PL	photoluminescence
PLE	photoluminescence excitation
STM	scanning tunneling microscopy (or microscope)
STS	scanning tunneling spectroscopy
TEM	transmission electron microscopy
UHV	ultra high vacuum

XAS	x-ray absorption spectroscopy
XRD	x-ray diffraction
XPS	x-ray photoemission spectroscopy

1. INTRODUCTION

Si and Si-based electronic devices have been dominating the microelectronic market for many decades. However, crystalline Si (c-Si) has not been successfully put into use in active optoelectronic devices, due to its indirect energy gap of about 1.1 eV. Because of conservation of momentum, indirect transitions in k space utilize phonons to conserve momentum. Figure 1.1 shows a schematic representation of a typical indirect process in c-Si.

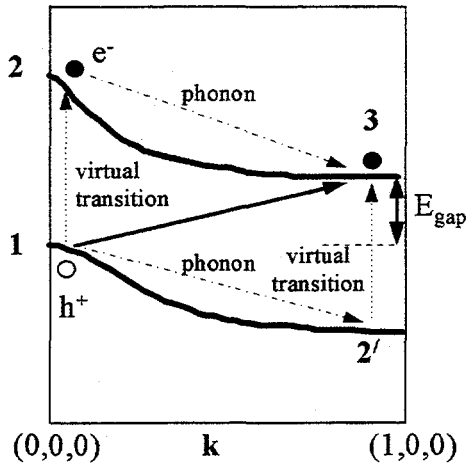

Figure 1.1 Schematic representation of the indirect absorption process in c-Si. The indirect transition can take an electron from state 1 to state 3 through two mechanisms. One mechanism involves a virtual photon transition from 1 to 2 at k = (0,0,0) and a phonon scattering of the electron from 2 at k = (0,0,0) to 3 at k = (1,0,0). A second mechanism (1 to 2′ to 3) involves a virtual optical transition at k = (1,0,0) and a hole scattering from k = (1,0,0) to k = (0,0,0). In both mechanisms, the final energy of the transition is E_{gap}.

Since there are two steps involved in an indirect transition, it is a second order perturbation process.[1] This is a very weak process in comparison with electric dipole allowed optical transition, which is a first ordered perturbation process. It is, therefore, expected that strong optical recombinations in the visible spectrum cannot be attainable from c-Si.

In order to realize optoelectronic applications within the well-known Si technology, the main approach has been to utilize the optical properties of III-V compounds such as GaAs or InP, leading to the field of heteroepitaxy on Si. Nevertheless, there still are efforts to overcome the weak emission in c-Si, by introducing point defects as recombination centers, or by relaxing the momentum conservation required in c-Si.[2] The requirement for momentum conservation is relaxed when the periodicity is removed locally or globally in Si. This occurs naturally at grain boundaries, line defects and other structural defects, as well as in amorphous Si. Periodicity can also be artificially destroyed by fabricating strained Si/Ge superlattices, or by producing spatially confined Si structures such as quantum wells, wires, or dots.

About six years ago, L. T. Canham reported the observation of a strong photoluminescence (PL) in porous Si under ultraviolet illumination at about room temperature.[3] Though many groups have confirmed the existence of strongly luminescent porous Si, obtained by electrochemical etching in dilute hydrofluoric

acid, the origin and mechanism of the luminescence remain controversial.[4-16] Some researchers attribute the PL to quantum confinement effects in the Si nanostructures.[3,6] Many others attribute it to amorphous Si,[11,12] siloxene (linear Si chains interconnected by oxygen or Si layers with alternating OH or H terminations, often written as $Si_6O_3H_6$),[8,13] hydrides/polysilanes (SiH, SiH_2, SiH_3, or $(SiH_2)_n$)[14,15] and oxygen related defect centers.[5,16] These alternative explanations for the observed visible luminescence in porous Si are based on the fact that the above mentioned Si related compounds have been documented to yield strong visible luminescence at room temperature. The luminescence properties from these species also show many similarities to luminescing porous Si. Consensus is difficult to reach because of the coexistence of a large variety of surface chemistries and structures in the porous Si system.

In order to shed more light on this matter, it seems useful to first examine more controllable systems, such as silicon nanocrystals (nc-Si), with well-controlled surface chemistry, structures, and sizes, and amorphous silicon oxide nanostructures (an-SiO_x), whose luminescence properties have some similarities to porous silicon . This work examines Si nanoclusters, with average size of a few nanometers, synthesized in ultra high vacuum (UHV) condition by pulsed laser deposition and physical thermal vaporization in a buffer gas. The different features of the nanoclusters obtained from these techniques are compared. The best technique is chosen to produce nc-Si with small size distribution and an-SiO_x

in a well-controlled environment for further study. Size, shape, composition and crystallinity of synthesized nc-Si are presented. The effects of surface passivation of nc-Si of different sizes with hydrogen or oxygen at different temperatures on the observed luminescence are described. Photoluminescence excitation (PLE) spectra and PL decay times of nc-Si and an-SiO_x are reported. Most recent results on the L-edge absorption spectra of nc-Si are analyzed. A comparison of the many different and common PL properties among the passivated nc-Si and an-SiO_x is included. Finally, it will also be discussed how this comparison leads to a model involving absorption mainly in the quantum confined Si cores, and emission due to transitions between defect states in the passivation layers. [7,9,10]

1.1 Quantum confinement effects in nanometer scale Si dots

Semiconductor dots with average size of a few nanometers are also called quantum dots or 0-D structures, due to the three dimensional confinements in such structures. If the semiconductor dots have spherical shapes and are embedded in a large band gap insulator host matrix such as SiO_2, the carriers in such dots behave similarly to the charged particles in infinite depth spherical potential wells. The theoretical treatment of such a problem- assuming the energy bands to be parabolic and the semiconductor to be described adequately by the effective mass

approximation- has been reviewed by A. D. Yoffe.[17] The Hamiltonian for such a system can be written as:

$$H = -\frac{\hbar^2}{2m_e}\nabla_e^2 - \frac{\hbar^2}{2m_h}\nabla_h^2 - \frac{e^2}{\varepsilon\,|\vec{r}_e - \vec{r}_h|} \qquad (1)$$

Here m_e and m_h are the effective mass of the electron and hole respectively, and ε is the static dielectric constant of the semiconductor. The first two terms in equation [1] represent the kinetic energies for the electron and the hole. The last term represents the Coulomb interaction between the electron and the hole. This Coulomb interaction term is responsible for the formation of excitons, bound states of electrons and holes. For bulk semiconductor, this last term can be ignored at room temperature (~ 25 meV), since the exciton energies of most semiconductors are less than 25 meV.[18] However, in a spatially confined structure, when the radius of the dot is smaller than the Bohr radius, the electron and hole pairs in excitons are pushed closer together according to $|\vec{r}_e - \vec{r}_h|$, and the exciton energies increase. So, for quantum wells, wires and dots, the increase in binding energies may leads to resolved exciton peaks at room temperature.[19] The energy difference between an electron in the conduction band and a hole in the valence band, corresponding to the Hamiltonian in equation [1], with the Coulomb term treated as a perturbation is:[17]

$$E(R) = E_g + \frac{\hbar^2}{2R^2}\left[\frac{\left(\alpha_{nl}^e\right)^2}{m_e} + \frac{\left(\alpha_{nl}^h\right)^2}{m_h}\right] - \frac{1.8\ e^2}{\varepsilon\ R} \qquad (2)$$

Here E_g is the bulk band gap, R is the radius of the spherical potential well, and α_{nl} is the n^{th} root of the spherical Bessel function of order l. Equation [2] shows that as the radius of the dot decreases, the energy difference between an electron in the conduction band and a hole in the valence band increases; and that the energy levels of the dot become discrete. A schematic diagram representing the discrete nature of the energy levels in quantum dots, and the increase in the energy difference between electrons in the conduction band and holes in the valence band in these dots as a function of spatial confinement is shown in figure 1.2:

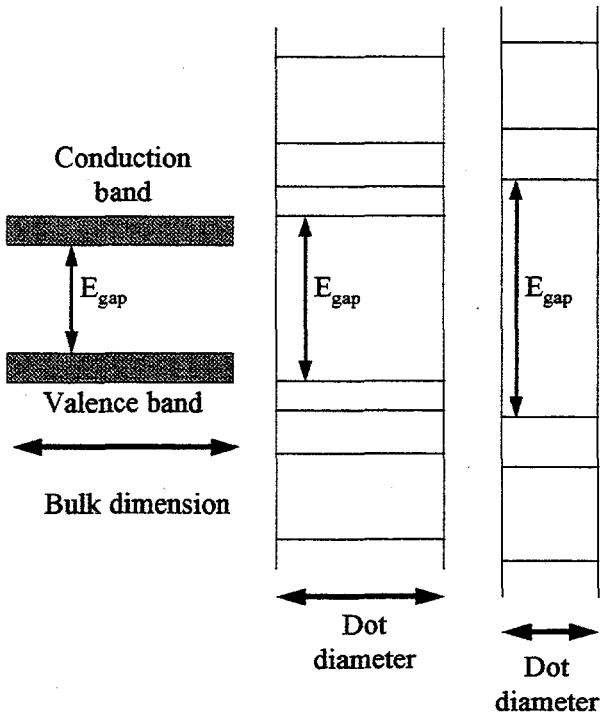

Figure 1.2 Schematic diagram representing the discrete nature of the energy levels in quantum dots, and the increase in the energy difference between electrons in the conduction band and holes in the valence band in these dots as a function of spatial confinement.

1.1a The effect of a finite well potential

It is probably more realistic to treat the electrons and holes in quantum dots embedded in an insulator host matrix as charged particles in finite depth potential wells. The implication of this is that the wavefunctions of the particles now penetrate the barriers at the interface with the matrix, and electron leakage from the dots is possible. In addition, analogous to the problems of an electron in an infinite square well potential and an electron in a finite square well potential,[20] the energy levels of charged particles in finite depth potential wells are lower than the ones in infinite depth wells. This implies smaller PL blueshifts, due to smaller increase in energy gaps, from quantum dots in finite depth wells in comparison with the ones in infinite depth wells.[21] Figure 1.3 shows a schematic diagram of the energy levels and eigenfunctions of conduction band electron of CdS, in a finite depth spherical potential well of $V_0 = 3.6$ eV, for a dot with radius of 1.5 nm, adapted from reference [21]. The arrows refer to the energy levels for $V_0 = \infty$.

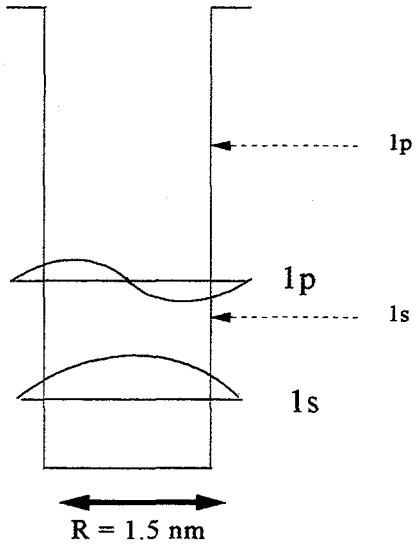

Figure 1.3 Energy levels and eigenfunctions of conduction band electron of CdS, in a finite spherical potential well with $V_0 = 3.6$ eV. Arrows show the energy levels for $V_0 = \infty$. Adapted from reference [21].

1.1b Quantum efficiency of optical transitions

The density of carriers is the same in quantum dots as in the corresponding bulk semiconductor. Nevertheless, the concentration of electrons and holes in fewer k-states in the dots, due to the quantization of the energy levels, results in higher quantum efficiency for allowed optical transitions.[19]

The expression for the oscillator strength f, which is the measure of the relative probability of a quantum mechanical transition, is written as:[17]

$$f \propto \Delta E |M|^2 |U|^2 \rho \qquad (3)$$

Here, ΔE is the transition energy, M is the transition dipole moment, ρ is the density of states term, and $|U|^2$ is concerned with the probability of finding an electron and a hole on the same site (the overlap). In quantum dots, the confinement of carriers in real space causes their wavefunctions to spread out in momentum space and a relaxation of momentum requirement. These increased overlaps enhance the oscillator strengths. So, in general, as the size of nanocrystallites is reduced, the quantum efficiency of optical transitions gets improved.

1.1c The effect of surface states

As the size of the quantum dots gets smaller, the surface to volume ratio of the dots gets bigger. Surface states, therefore, may play an important role in determining the electronic properties of the quantum dots.

Since the symmetry experienced by the atoms inside a nanocrystal is disrupted at the surface, the surface atoms may have wavefunctions and energy levels that are forbidden to bulk atoms. This indicates the possible existence of sub band gap energy levels associated with surface states. A schematic diagram showing the energy levels of a quantum dot near the band gap, including sub-band gap energy levels associated with surface states, is shown in figure 1.4. These sub-band gap states are not very desirable, since electrons and holes may relax to these states prior to optical recombinations. One direct consequence of this is a reduction in PL blueshifts observed from quantum dots with high density of surface states.

Here, dangling bonds (electron deficient bonds) should be mentioned as a special case associated with surface states. Dangling bonds pose a serious problem for quantum dots synthesized in UHV condition. These bonds just stick out into vacuum with nothing to bond to. Surface reconstruction, in many cases, reduces the density of dangling bonds, but usually do not completely eliminate them. As a result, these bonds may act as nonradiative recombination centers for carriers generated in the dots.[22,23] If these dangling bonds are not passivated (bonded to other atoms such as hydrogen, or oxygen...), they can efficiently quench PL from quantum dots.

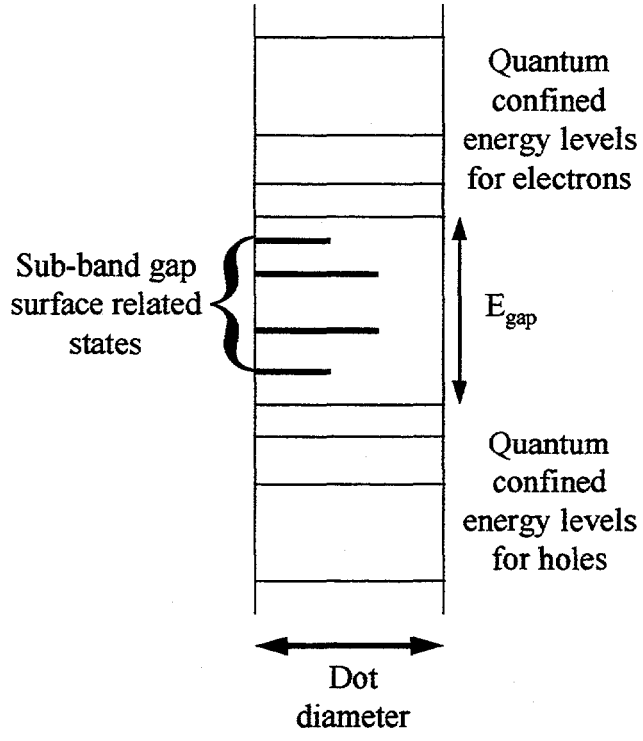

Figure 1.4 A schematic diagram showing the energy levels of a quantum dot near the band gap, including sub-band gap energy levels associated with surface states.

2. EXPERIMENTAL PROCEDURE AND APPARATUS

In this chapter, the apparatus and experimental procedure is discussed. Brief descriptions of the physics behind the techniques are also given.

2.1 Synthesis and analysis chamber

The synthesis and analysis chamber was a UHV chamber, pumped by a 300l/s ion pump, with a base pressure of about 2-5× 10^{-10} Torr. This chamber is equipped with a fused silica window for *in situ* optical spectroscopies, and a host of surface analysis instruments. Among these are a Mc Allister UHV scanning tunneling microscope (STM) with a Nanoscope III electronic controller from Digital Instruments, Inc., a quadrupole mass spectrometer for residual gas analysis, electron gun, x-ray source, and a double pass cylindrical mirror analyzer for Auger electron spectroscopy (AES) and X-ray photoelectron spectroscopy (XPS) from Perkin Elmer, Inc.. A schematic diagram of this chamber is illustrated in figure 2.1.

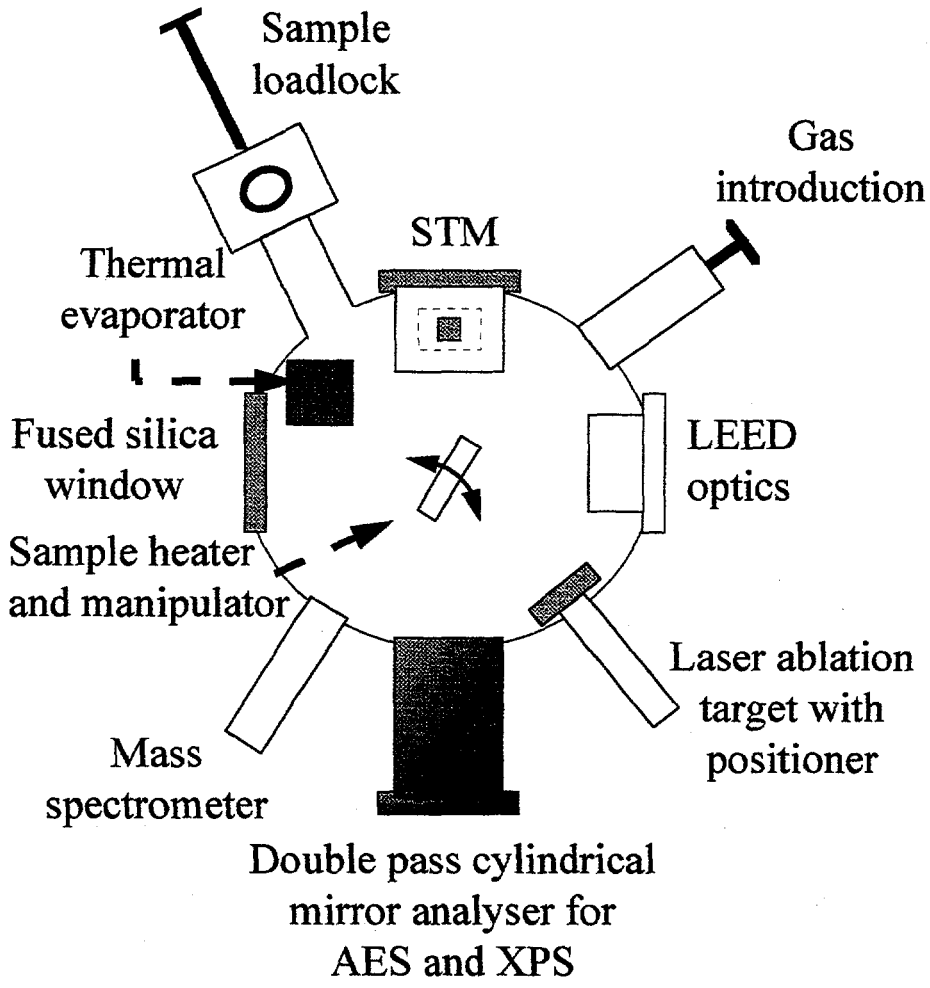

Figure 2.1 A schematic diagram of the synthesis and analysis chamber used in this experiment.

2.2 Auger electron spectroscopy (AES)

In AES, one determines the elemental composition at the surface of a sample by measuring the energy distribution of Auger electrons emitted during irradiation with a beam of energetic electrons.[24] When a core level electron is knocked off the sample by a high energy electron from the electron gun, an electron from an outer

level will relax down to this vacant core level. The energy gained by this transition is either emitted as radiation or given to another electron to eject it out of the sample. This ejected electron is called an Auger electron. Since the energies of the emergent Auger electrons are determined by the differences in the binding energies associated with the deexcitation of atoms, AES is an element specific technique. As with other electron spectroscopies, the observation depth in AES is about 1- 4 nm, and is determined by the electron escape depth. A KL_1L_2 Auger transition is depicted in figure 2.2.

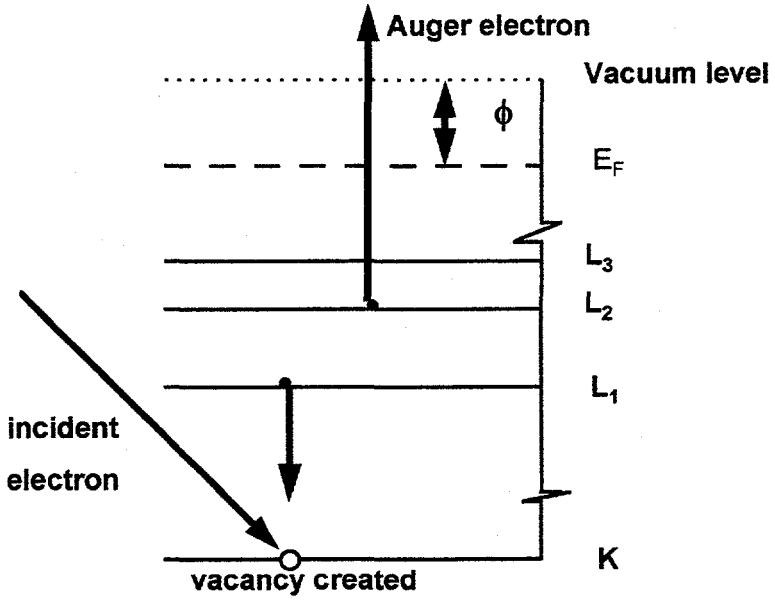

Figure 2.2 A KL_1L_2 Auger transition.

The kinetic energy of the Auger electron in this transition is:

$$K.\,E. = E_k - E_{L_1} - E_{L_2} - \phi \qquad (4)$$

where E_k is the binding energy of an electron at level k, and ϕ is the work function of the sample. If the analyzer used to detect the Auger electrons has a work function of ϕ_A, then the kinetic energy of a KL_1L_2 Auger electron as measured by the analyzer is:

$$K.E._{measured} = E_k - E_{L_1} - E_{L_2} - \phi_A \quad (5)$$

The Auger peak amplitude for a given sample is determined by the initial core level ionization cross section. This dependence is conventionally tabulated as the sensitivity factor. The different Auger peaks in an AES spectrum are usually divided by the corresponding sensitivity factors so that a quantitative comparison of the different Auger amplitudes obtained from a sample is possible.

In this thesis, AES is employed primarily to monitor the cleanliness of the substrates, and the compostion of the nanoclusters at different stages of the experiment.

2.3 X-ray photoelectron spectroscopy (XPS)

In XPS, one ejects electrons out of a sample by exciting it with a high energy photon source such as x-rays produced by electron bombardment of Mg or Al targets.[24] When the incoming photon energy hν is shined onto a sample, many

electrons of the sample are excited. Some of these electrons may acquire enough energies to escape from the sample with kinetic energies given by:

$$K.\,E. = h\nu - E_b - \phi \qquad (6)$$

where E_b is the binding energy of the escaping electron, and ϕ is the work function of the sample. A schematic diagram depicting the photoelectric effect in XPS is given in figure 2.3.

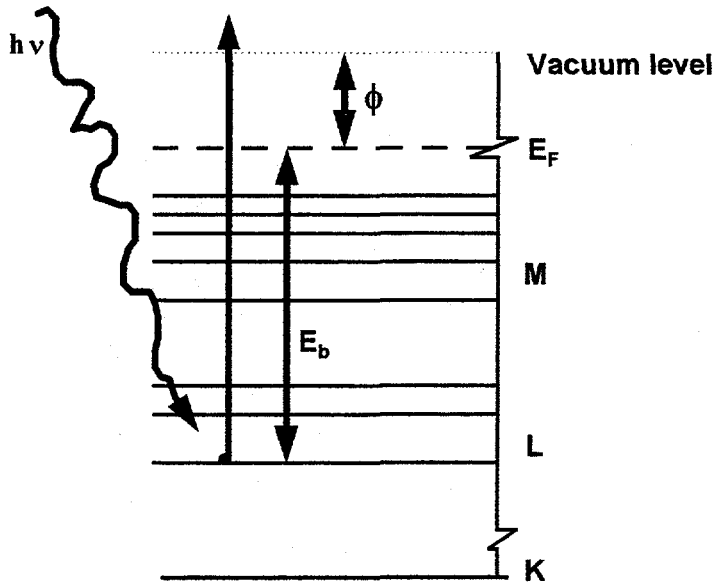

Figure 2.3 A schematic diagram showing the photoelectric effect in XPS.

If the analyzer used to detect photoelectrons has a work function ϕ_A, then the binding energies of the detected photoelectrons are given by:

$$E_b = h\nu - K.\,E._{measured} - \phi_A \qquad (7)$$

So like AES, XPS can be used to identify elements uniquely. In addition, the binding energies of electrons in an atom shift in unison with chemical changes,

chemical shifts are evident in both AES and XPS spectra. However, line widths are broader and the chemical shifts are more difficult to interpret in the three electrons Auger process than in the one electron photoelectric process. Consequently, XPS is typically used to explore changes in chemical bondings.

In this thesis, XPS is employed primarily to monitor the chemical changes at the surface of the Si nanoclusters.

2.4 The scanning tunneling microscope (STM)

The STM exploits the ability of electrons to tunnel through thin barriers to produce sharp surface images. A schematic diagram of the STM equipped on our UHV chamber is shown in figure 2.4a.

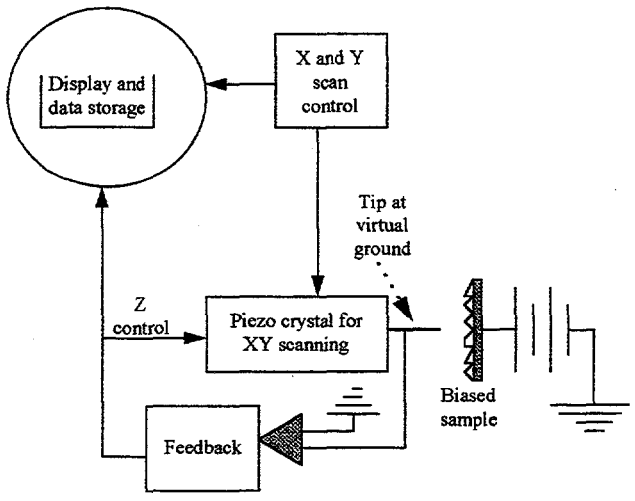

Figure 2.4a A schematic diagram of the STM used in this experiment.

In this system, a bias voltage is applied to the surface under study, which is about 0.5-2 nm away from a probe tip at a virtual ground. The resulting tunneling current is measured, and maintained with the help of a feedback loop which controls the tip to sample distance by adjusting the length of a cylindrical piezoelectric crystal. If an electric field is applied to such a crystal, strain is induced and atomic scale changes in the crystal's physical dimensions follow. The maximum range of motion for this STM is 1.4 μm in the x and y directions, and 0.4 μm in the z direction. In operation, the tip is scanned over the sample's surface and the z position as a function of x and y is recorded.

As described above, the lateral resolution of an STM image is a product of the convolution of the real surface information with the tip's shape, due to its finite radius of curvature. Nevertheless, because of the exponential dependence of the tunneling current on the distance between the tip and the surface, unless the tip is fairly blunt, only one or two atoms sitting right at the top of the tip contribute significantly to the tunneling current. Atomic resolution images of flat surfaces are, therefore, easily obtained with the STM. However, the same may not be assumed for STM images of rough surfaces, or of nanoclusters on flat surfaces. Because of the finite radius of the tip, the tunneling current may be substantial even when the tip is not directly above the rough features or the nanoclusters. The net result is that the sizes of rough features or nanoclusters on surfaces obtained by STM are bigger than their true values. This point is illustrated in figure 2.4b. Even so, this problem

could be reduced if one raises the STM tip as high above the substrate as one can during the operation of the STM without losing the image under examination.

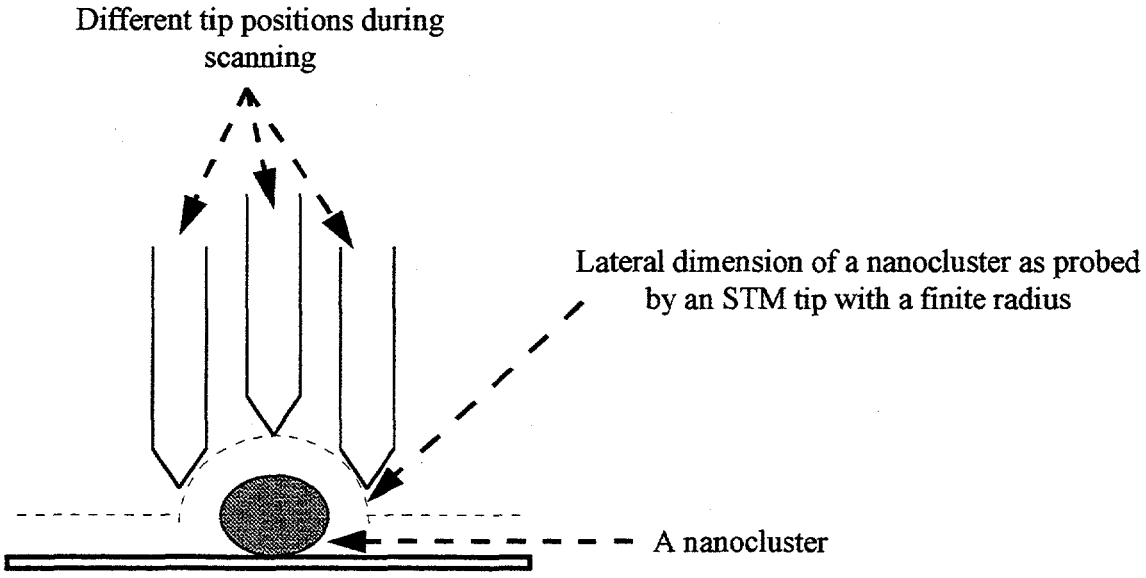

Figure 2.4b Lateral dimension of a nanocluster as scanned by an STM tip with a finite radius.

Since the piezoelectric crystal can move the STM tip vertically with sub-atomic accuracy, the vertical resolution of an STM image ultimately depends on the nature of the quantum mechanical tunneling current between the tip and the sample.

In figure 2.4c, an energy diagram near a negatively biased semiconductor sample and a STM tip is drawn. In this figure, E_{FS}, E_V, E_C, ϕ_S are the Fermi level, top of the valence band, bottom of the conduction band, and work function of the negatively biased semiconductor sample respectively; similarly E_{FM} and ϕ_m are the Fermi level and work function of the metal tip.

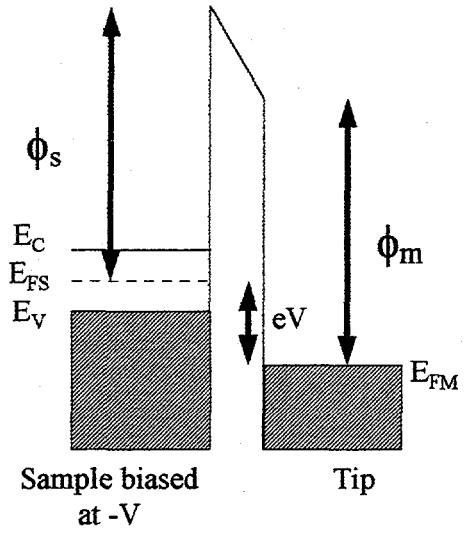

Figure 2.4c An energy diagram near a negatively biased semiconductor sample and a STM tip.

Assuming that the density of states and work functions of the tip and the sample are uniform , the Wentzel-Kramers-Brillouin (WKB) theory predicts that the tunneling current is given by:[25]

$$I = \int_0^{eV} \rho_s(E)\rho_m(E - eV)T(E,eV)dE \qquad (8)$$

Here ρ_s and ρ_m are the densities of states of the sample and tip at energy E, measured with respect to their individual Fermi levels. T(eV,E) is the tunneling transmission probability for electrons with energy E and applied bias voltage V. Here, for a negative sample bias: eV<0, and for a positive sample bias: eV>0. To

be consistent with figure 2.4c, from here on only negative sample bias is considered. Nonetheless, the analysis is analogous for positive sample bias.[25,26] Since the density of states of a metal tip is relatively structureless in comparison with with the density of states of a semiconductor, it may be moved outside the integral:

$$I \propto \int_0^{eV} \rho_s(E) T(E, eV) dE \tag{9}$$

$$\text{with } T(E, eV) = \exp\left(-2\frac{s}{\hbar}\sqrt{2m\left(\frac{\phi_S + \phi_m}{2} + \frac{eV}{2} - E\right)}\right) \tag{10}$$

where s is the sample to tip distance.

Examination of the transmission probability T shows that T is largest for electrons at the Fermi level of the negatively biased electrode. And so, to a qualitative level, one can write:

$$I \propto \rho_s(E_{FS})\, T(E_{FS}, eV) \tag{11}$$

If free electron mass, and work functions of a few eV are used in equations [10] and [11] then:

$$I \propto \rho_s(E_{FS}) \frac{1}{\exp(10^{10} s)} \tag{12}$$

where the unit of s in equation [12] is meter.

From equation 12, it is clear that the tunneling current changes by a factor of 2 or 3 for a sub-atomic change in the tip to sample distance. This explains why the STM can produce images with atomic resolution in the vertical direction.

In addition, it follows from equation [9] that:[26]

$$\frac{dI/dV}{I/V} = \frac{\rho_s(eV)T(eV)}{\frac{1}{eV}\int_0^{eV}\rho_s(E)T(E)dE}$$

Since the transmission probability appears both in the numerator and denominator, then, to first order, one can write:[26]

$$\frac{dI/dV}{I/V} \approx \frac{\rho_s(eV)}{\frac{1}{eV}\int_0^{eV}\rho_s(E)dE} \tag{13}$$

According to equation [13], the normalized conductance is related to the normalized density of states of the surface under study. So, by keeping the tip to sample distance fixed while ramping the bias voltage from some negative value to some positive value (usually from -3 V to +3 V), one may obtain the normalized density of states of the valence band and conduction band of a semiconductor sample, through measuring the normalized conductance. This mode of operation is called scanning tunneling spectroscopy (STS). Actually, the above derivation is only an approximation to the true density of states of a semiconductor sample. A more elaborate calculation for a general case yields:[25]

$$\frac{dI/dV}{I/V} = \frac{\rho_s(eV)\rho_m(0) + \int_0^{eV}[\frac{\rho_s(E)\rho_m(E-eV)}{T(eV,eV)}][\frac{dT(E,eV)}{dV}]dE}{\frac{1}{eV}\int_0^{eV}\rho_s(E)\rho_m(E-eV)[\frac{T(E,eV)}{T(eV,eV)}]dE}$$

$$\text{or } \frac{dI/dV}{I/V} = \frac{d(\log I)}{d(\log V)} = \frac{\rho_s(eV)\rho_m(0) + A(V)}{B(V)} \tag{14}$$

where A(V) and B(V) vary slowly with bias voltage. Thus, great care must be made in any quantitative interpretation of the normalized conductance curve.[25]

In this thesis, a Mc Allister UHV STM, with a Nanoscope III electronic control, was employed mainly to obtain the size distribution of the synthesized Si nanoclusters. STS technique was experimented on atomically flat HOPG surfaces and HOPG surfaces with deposited Si nanoclusters. Even though the density of states obtained from STS for HOPG flat surfaces is repeatable and is consistent with literature, the same cannot be said for the results on Si nanoclusters. This point will be discussed in more details in the next chapter.

2.5 X-ray diffraction

In x-ray diffraction, one can determine the crystallinity and average grain size of a sample by analyzing the superposition of x-rays scattered elastically by the individual atoms of the sample.

If the sample is crystalline, the condition for constructive interference of the radiation from successive planes in a certain direction is given by the Bragg law, and illustrated in figure 2.5a:

$$2d \sin\theta = n\lambda \qquad (15)$$

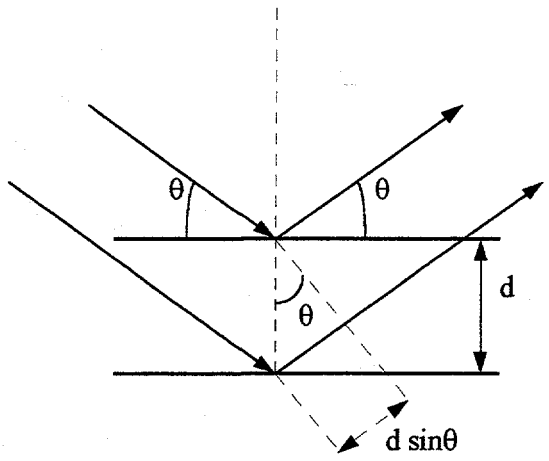

Figure 2.5a Illustration of the Bragg equation. The spacing of parallel atomic planes is labeled as d, and n is an integral number.

As can be seen from equation [15], Bragg reflection can occur only for wavelength $\lambda \leq 2d$. This is why x-ray is needed to observe Bragg reflection. In addition, each plane reflects only 10^{-3} to 10^{-5} of the incident radiation, Bragg law is, thus, a consequence of the long range periodicity of the lattice. So, constructive and destructive interference of the scattered light cannot happen for amorphous or disordered materials, since their structures do not have the long range periodicity needed for the Bragg reflection. This is why one can use XRD to determine whether a sample is crystalline or not.

The instrument for studying crystalline (and noncrystalline) materials by measurements of the way in which they diffract x-rays of known wavelength is usually called a diffractometer. In the diffractometer, the intensity of a diffracted

beam is measured directly, either by means of the ionization it produces in a gas or the fluorescence it produces in a solid. The essential features of a diffractometer are shown in figure 2.5b. A specimen C is supported on a table H, which can be rotated about an axis O perpendicular to the plane of the drawing. The x-ray source is S. X-rays diverge from this source and are diffracted by the specimen to form a convergent diffracted beam which comes to a focus at the slit F and then enters the counter G. A and B are special slits which define and collimate the incident and diffracted beams. The support E and H are mechanically coupled so that a rotation of the counter through 2x degrees is automatically accompanied by a rotation of the specimen through x degrees.

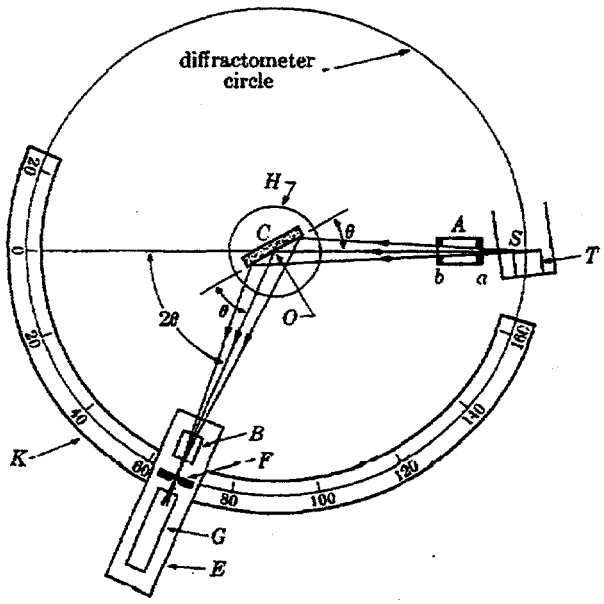

Figure 2.5b A chematic diagram of a diffractometer, taken from reference [27].

Since each reflecting plane reflects only 10^{-3} to 10^{-5} of the incident radiation, there is a need for a minimum number of parallel diffracting planes to observe sharp interference effect. As this number falls below the minimum, in other words, as the particle size decreases below about 10^{-5} cm, it follows that the interference is less perfect and the diffraction peaks (as recorded by the diffractomoter) will become broader. From the broadening of the diffraction peaks, one can calculate the average diameter of the nanocrystals from the sample through the Scherrer formula:[27]

$$d = \frac{0.9\lambda}{B\cos\theta} \tag{16}$$

where B is the full width at half maximum (FWHM) of the diffraction peak measured in radians, λ is the wavelength of the x-ray beam and θ is the Bragg angle under study. To be more accurate: $B^2 = B_m^2 - B_S^2$ where B_m is the FWHM of the diffraction peak of Si nanocrystals, and B_S is the FWHM (due to instrumental resolution and x-ray linewidth) of the diffraction peak of standard Si large grain microcrystals (> 10 microns).

In this thesis, *ex situ* XRD measurements, using the Cu $K\alpha_1$ line from a Rigaku 300ELR with rotating anode diffractometer, were performed on Si films deposited on glass slide. XRD was employed, here, to study the crystallinity and average size of the synthesized Si nanoclusters.

2.6 Transmission electron microscopy (TEM)

In TEM, one can study the crystallinity and size distribution of particles in a sample by analyzing the diffraction or transmission of high energy electrons (between 50 and 100 keV) from a specimen.

A TEM is composed of the following major sections: electron gun, condenser lens, specimen holder, objective lens, projector lens, viewing and photographing chamber. The electron gun generates the electron beam which illuminates the object. The condenser lens or lenses increase the electron density reaching the specimen by concentrating the beam. The objective lens provides the first magnification. The projector or image lens selects a small portion of the intermediate image produced by the objective lens and magnifies it again. All the lenses in a TEM are either magnetic or electrostatic lenses. The viewing chamber at the bottom of the microscope contains a fluorescent viewing screen or a photographic plate. A schematic diagram of a TEM, adapted from reference [28], is shown in figure 2.6 below:

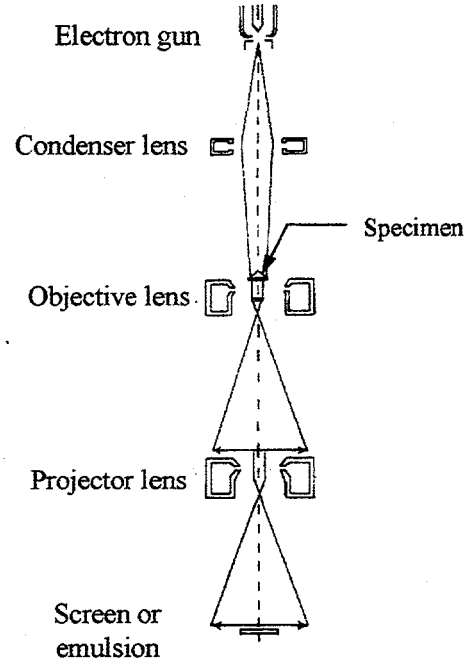

Figure 2.6 A schematic diagram of a TEM, adapted from reference [28].

The resolving power of a light microscope is limited by the wave nature of the radiation. The effect of this is that two separate points cannot be resolved as separate unless their centers are the distance d apart, whereby d is the radius of the Airy disc referred to the object plane:

$$d = \frac{0.5\lambda}{n \sin\alpha} \tag{17}$$

where $\lambda =$ wavelength of the illuminating light, $n =$ index of refraction of the medium between object and lens, $\alpha =$ aperture of lens (half angle of collected light beam), $n \sin\alpha$ = numerical aperture of the lens (0.95 at maximum in air). Even if

one uses the ultra-violet line of mercury ($\lambda = 253.7$ nm), oil immersion optics ($n \sin\alpha = 1.4$), and quartz lenses, the best resolution obtainable from the light microscope is only about 100 nm.

The electron microscope makes use of the wave properties of the moving electron. Its "de Broglie" wavelength is:

$$\lambda = \frac{h}{mv} = \frac{1.23}{V^{1/2}} \text{ [nm]} \qquad (18)$$

where h = Planck's constant, m = mass of electron, v = velocity of electron, and V = accelerating voltage in volts. For electron with V = 50 kV, the wavelength is about 0.00535 nm. This is about 10^5 times shorter than the wavelength of light, and is much smaller than the interatomic spacing in a solid. However, due to aberrations, the best practical resolution is between 0.5 and 1 nm.

Three types of electrons emerge after transit through a specimen: unscattered electrons, elastically scattered electrons, and inelastically scattered electrons. The unscattered electrons are those that do not interact with the atoms of the specimen. The elastically scattered electrons interact with the nuclei of atoms in their path. The elastically scattered electrons do not lose kinetic energy but change their direction significantly, due to diffraction or incoherent scattering. The inelastically scattered electrons interact with the electrons of the atoms in their path and tend to degrade the image. The TEM image is formed essentially by the scattering of electrons during their passage through the specimen. Those sections that are

denser or thicker or are composed of heavier atoms will scatter more electrons and will, therefore, appear darker in the final image on the fluorescent screen. They will be lighter on the photographic plate.

If the sample is crystalline, at some suitable angle, many electrons are Bragg reflected, and the image formed by the transmitted electrons shows clear corresponding lattice fringes right on it. Of course, TEM can also be used in diffraction mode as in XRD. Nonetheless, electron diffraction is more surface sensitive than XRD, due to the small electron escape depths.

In this work, the TEM was carried out *ex situ* by Dr. Margaret Olsen on a JEOL JEM4000EX instrument operating at 400 kV accelerating voltage. Samples were taken out of the synthesis chamber and prepared by gently scraping the Si film off its substrate surface using a blunt scalpel taking care not to scratch the substrate itself. The film was then collected onto an amorphous carbon coated Cu TEM grid. Here, TEM was employed to study the crystallinity and size distribution of clusters passivated with oxygen or exposed to air for a long time. Clusters which are heavily surrounded by insulator such as silicon oxide cannot be imaged by the STM, and XRD is not sensitive enough to probe the crystallinity of a thin film of Si nanopowder of a few ten of nanometers.

2.7 Photoluminescence spectroscopy

2.7a Photoluminescence spectroscopy

Photoluminescence (PL) spectroscopy refers to the emission of optical radiation resulting from non thermal excitation of the energy levels of atoms, molecules, polymers, and crystals through absorption of light.

The PL setup used in this work is shown in figure 2.7.

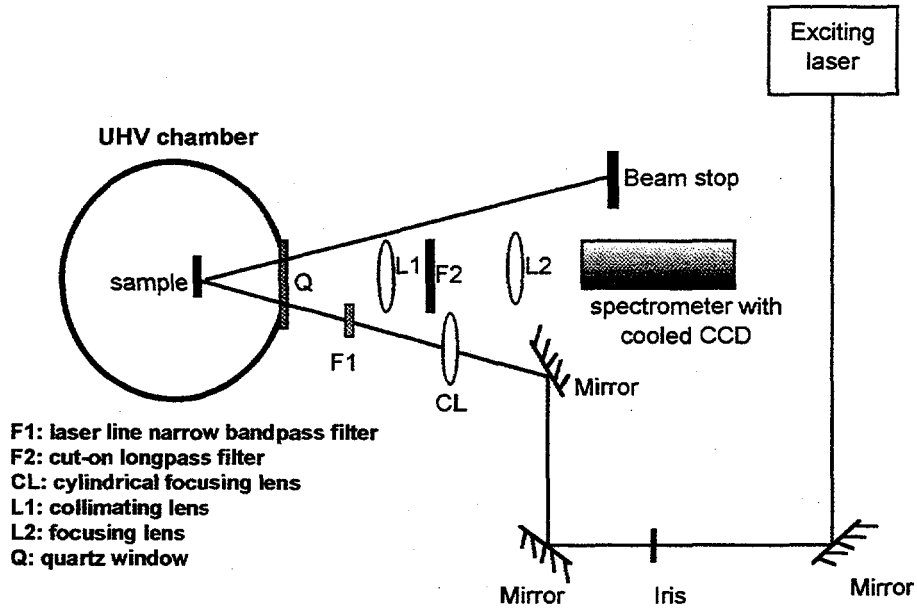

Figure 2.7 PL setup.

In this set up, the excitation source is either a 15 mW, 325 nm continuous wavelength He-Cd laser (Omnichrome, series 56), or a Spectra Physics Ar ion laser operating at 488.8 nm. The incoming laser beam was passed through a narrow band pass filter, in order to remove higher order components of the laser light as well as unwanted scattered light generated by the plasma inside the laser, before reaching the sample inside the UHV chamber. A fraction of the

luminescence from the sample was collimated by lens L1 and then focused by lens L2 onto the slit of a grating spectrometer (Oriel Multispec). A long pass filter was situated in between lens L1 and lens L2 to prevent the scattered exciting laser light from entering the spectromoter slit. PL spectra were recorded by an Oriel Instaspec IV cooled charged-coupled Si detector array. All PL spectra have been corrected for instrument response using a calibrated lamp traceable to NIST standards.

Almost all excited electrons and holes drop quickly to the conduction band mimimum and the valence band maximum respectively, or to the sub-band gap traps by nonradiative processes prior to optical transitions. PL spectroscopy is, therefore, a useful tool in investigating the optical band gaps as well as sub-band gap energy levels in semiconductor nanocrystals. In this thesis, PL spectroscopy was employed to obtain the emission spectra from Si nanoclusters of various sizes and surface chemistries.

2.7b Photoluminescence excitation (PLE) spectroscopy

A PLE spectrum is the curve obtained when the luminescence of a sample is measured as a function of the excitation wavelength. PLE spectroscopy is useful in studying relative transition rates from various energy levels. For a film much thinner than the absorption length of the exciting light, the PLE spectrum is proportional to the absorption coefficient of the film. Moroever, if the PL intensity

of a thin sample, I_{PL}, is linearly proportional to the exciting laser beam intensity, I_o, then:

$$I_{PL} \approx QI_o[1-\exp(-\alpha\ x)] \tag{19}$$

$$\approx QI_o\alpha\ x \text{ (for } \alpha\ x << 1) \tag{20}$$

$$\approx QI_o \text{ (for } \alpha\ x >> 1) \tag{21}$$

where α is the absorption coefficient of the film and Q is a proportionality constant.

For PLE measurements, white light from a 1 kW mercury-Xenon arc lamp was passed through appropriate order selection filters and then focused onto the input slit of a monochromator. Monochromatic light from the output of the monochromator was then used to excite the luminescence from the sample. A broadband optical detector monitored the energy flux at the output of the monochromator, and this was used to normalize the PLE spectra for the variation of intensity as a function of excitation energy. Luminescence from the sample was collected using the same optics as in PL spectroscopy.

In this thesis, PLE spectroscopy was employed to investigate the absorption mechanism in Si nanocrystals and SiO_x nanostructures.

2.7c Photoluminescence decay (PL decay) spectroscopy

The knowledge of the PL lifetime as a function of the emitted photon energy can help to determine the luminescence mechanism.

The PL decay is formulated as: $I_{PL} = Ae^{-t/\tau}$ (22)

If there are competing relaxation processes with lifetimes of τ_1, τ_2, and τ_3, then:

$$I_{PL} = Ae^{-[t(\frac{1}{\tau_1}+\frac{1}{\tau_2}+\frac{1}{\tau_3})]} \quad (23)$$

This corresponds to a monoexponential decay pattern in which the relaxation process with the shortest lifetime dominates.

If there are independent relaxation processes with lifetimes of τ1, τ2, and τ3, then:

$$I_{PL} = A_1e^{-t/\tau_1} + A_2e^{-t/\tau_2} + A_3e^{-t/\tau_3} \quad (24)$$

where $A_1, A_2,$ and A_3 are some proportionality constants. This corresponds to a multiexponential decay, which is expected for interband radiation transitions from nc-Si with a size spread. A nonexponential decay may also be an indication of a distribution of lifetimes which are typical of radiative transitions between broad bands of localized states.

The setup for PL decay spectroscopy is similar to that of a PL spectroscopy, except that the exciting source is replaced by a pulsed laser, and the detector is substituted by a photomultiplier tube. In this work, an excimer laser (Questek, series 2000) operating at 308 nm with a pulse duration of 20 ns was used for excitation. A Hamamatsu photomultiplier tube with GaAs photocathode, providing extended red response, and a rise time of 12 ns was used for detection at the output of the monochromator. Neutral density filters were employed so that the laser beam, upon striking a sample surface of a few mm^2, had an energy of a few μJ.

In this thesis, PL decay spectroscopy was employed to measure the lifetimes of Si nanoclusters of different sizes and surface passivations. These measurements, when compared with calculated radiative lifetimes of Si nanocrystals and measured lifetimes from luminescent compounds of Si such as siloxene or polysilanes ..., would shed light on the luminescence mechanism of the synthesized Si nanoclusters.

2.8 Pulsed laser deposition

Pulsed laser deposition was used in the early stage of this work to make Si nanoclusters. The mechanism of ablation is complex and still under debate. The most simple explanation for the ablation process of semiconductors by an excimer laser assumes the process of pulsed laser vaporization. Here, the absorbed light intensity, with a time and space dependent source term, is instantaneously converted to heat, which vaporizes material at the surface and diffuses according to the conventional heat diffusion equation. Reproduced from reference [29], that equation can be written as:

$$\frac{\partial T}{\partial t} = \frac{\alpha}{\rho C_p} I(z,t) + \frac{1}{\rho C_p} \frac{\partial}{\partial z} (\kappa \frac{\partial T}{\partial z}) \qquad (25)$$

In this equation, it is assumed that the laser beam is uniform in the x-y plane and travels in the z direction; that the target composition is homogeneous; and that the

cross section of the laser beam spot is greater than the heated sample's surface so that edge effects are negligible. *I(z,t)* is the power density of the laser light at depth *z* and time *t*. T, ρ, C_P, κ, and α are the temperature, density, specific heat at constant pressure, thermal conductivity, and absorption coefficient of the sample respectively. For a homogeneous absorbing medium the power density will be:

$$I(z,t) = I_o(t)(1-R)\exp(-\alpha\ z) \tag{26}$$

where $I_o(t)$ is the output power density from the laser and R is the target reflectivity. Assuming no temperature dependence of thermal and optical parameters, no phase change induced by the laser pulse, homogeneity along the z axis, constant laser power, and infinite sample thickness, the exact solution for equation (25) is:[29]

$$\begin{aligned} T(z,t) = \{&(2I_o/\kappa)(Dt)^{1/2}\, ierfc\left|z/2(Dt)^{1/2}\right| - (I_o/\alpha\kappa)\exp(-\alpha\ z) \\ &+ (I_o/2\alpha\kappa)\exp(\alpha^2 Dt - \alpha\ z)erfc\left|\alpha(Dt)^{1/2} - z/2(Dt)^{1/2}\right| \\ &+ (I_o/2\alpha\kappa)\exp(\alpha^2 Dt + \alpha\ z)erfc\left|\alpha(Dt)^{1/2} + z/2(Dt)^{1/2}\right|\}(1-R) \end{aligned} \tag{27}$$

If the light absorption length (α^{-1}) is small compared with the heat diffusion length $\sqrt{Dt} = \sqrt{\kappa\ t/\rho\ C_P}$, the solution can be simplified:

$$T(z,t) = [2I_o(Dt)^{1/2}/\kappa]\ ierfc[z/2(Dt)^{1/2}](1-R) \tag{28}$$

and for z = 0, i.e., at the sample surface,

$$T(0,t) = (2I_o/\kappa)(Dt/\pi)^{1/2}(1\text{-}R) \tag{29}$$

Equation (29) yields $T_{max} \approx 2500\ ^{\circ}C$ at the surface of a Si target, ablated by an excimer laser operating at 308 nm, with a power density of about 2×10^8 W/cm^2. However, it is worthy to note that actually equation (25) cannot be solved analytically for a general case, because in the semiconductor case, the thermal and optical parameters are temperature dependent and show strong variation with the phase (crystal, liquid, amorphous). Numerical calculation taking into account the mentioned dependency of thermal and optical parameters is neccessary, if accurate values are desired.

An indepth look at the mechanism of ablation[30] shows that if a plasma forms for any reason during laser-surface interaction in vacuum or air, then an explicit laser-plasma interaction begins. Ions in the plasma are accelerated to as much as 100-1000eV, and collisional sputtering results. [31] Repeated thermal shocks from the laser pulses may also cause flakes to detach from a target.[32] This is called exfoliational sputtering. Droplets of material may be formed and expelled from a target as a consequence of the transient melting by the laser pulse as well. This form of hydrodynamic sputtering has been observed in many metals, and is described in detail by Kelly and Rothenberg.[33] Many other secondary mechanisms are also reviewed in reference [30]. In addition, the surface morphology of the ablated target was observed to change after every single laser pulse. Therefore,

each pulse probably deposits different amounts of material with plume orientation falling off as cosine to the power of x ($x \geq 4$) along the target surface normal.[30]

The laser employed, in the experiment, was an excimer laser (using hydrogen cloride and xenon gas) producing output at a wavelength of 308 nm and a pulse duration of 20 nanoseconds. The laser beam was focused such that a peak power density of about 2-4 x 10^8 W/cm^2 was incident on a Si target, whose surface had been cleaned in UHV condition earlier on by laser pulses from the same laser at a peak power density of < 1 x 10^8 W/cm^2. The substrates used to collect Si nanoclusters were the basal planes of HOPG. These HOPG surfaces, which had been cleaved by peeling off layers of graphite with a piece of tape, were transfered into the UHV chamber through a loadlock. The substrates were then heated to 900 °C for 2 minutes to remove any absorbed surface contaminant, and were positioned 5 to 8 cm away from the Si target. These substrates were hidden away from the Si plumes generated by the laser pulses during the cleaning of the Si target. A schematic diagram representing the setup for the laser ablation deposition in this experiment is shown in figure 2.8.

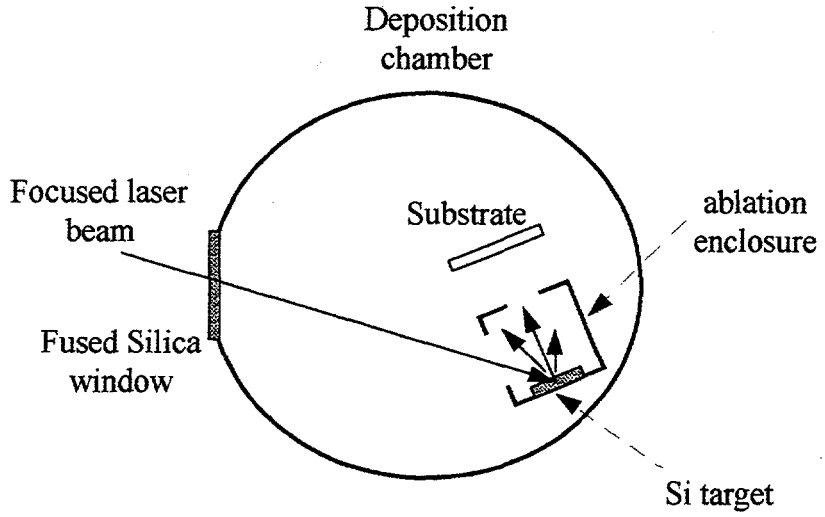

Figure 2.8 Laser ablation setup.

Si nanoclusters were synthesized by laser ablation in two different ways, as described in the following.

1) Laser ablation followed by substrate annealing:

In this method, a small amount of Si (less than a monolayer) is first deposited on a graphite substrate. The sample is then annealed so that Si atoms aggregate into clusters through surface diffusion. This technique is limited to the formation of less than one monolayer of clusters.

2) Laser ablation in an inert buffer gas:

In this method, the ablation process takes place in the UHV chamber which is to be filled with an inert buffer gas such as Ar, or He prior to deposition.... The inert buffer gas helps the vapor species from the ablated plume to undergo enough

collisions that nucleation and growth of these vapor species to form clusters can occur before their arrival at the substrate. For this method, samples with greater target to substrate distances, and/or deposited at higher inert buffer gas pressures have bigger clusters, since the vapor species undergo more collisions.

2.9 Gas Aggregation deposition

Gas aggregation deposition is another method to produce clusters.[34-36] In all cases, a liquid or a solid is evaporated at a high vapor pressure into a colder buffer gas. Following nucleation and condensation, the vapor phase is depleted, and thereafter cluster growth occurs by coagulation during the flight to the substrate.

A schematic diagram of the gas aggregation deposition set up used in this experiment is shown in figure 2.9a. In this setup, the chamber was filled with Ar gas up to the desired pressure. Pre-melted and outgassed Si inside a carbon boat (BN boat is a good alternative), which was fitted inside a W basket, was resistively heated up to a few hundred degrees above its melting point (as measured by an optical pyrometer). The substrates used to collect nc-Si powder were highly oriented pyrolytic graphite (HOPG) surfaces, glass slides, fused silica, or sheets of Mo or Ta. These substrates had been cleaned *in situ* inside a UHV chamber by flash heating up to 900 °C before they were positioned about 5 to 8 cm directly above the evaporation boat. A manually operated shutter was placed in between

the evaporation boat and the substrate holder to control the Si arrival fluences. The average size of the Si clusters synthesized by this technique could be varied by increasing (or decreasing) the Si source temperature, the Ar buffer gas pressure, the source to substrate distance, or a combination of all these parameters.

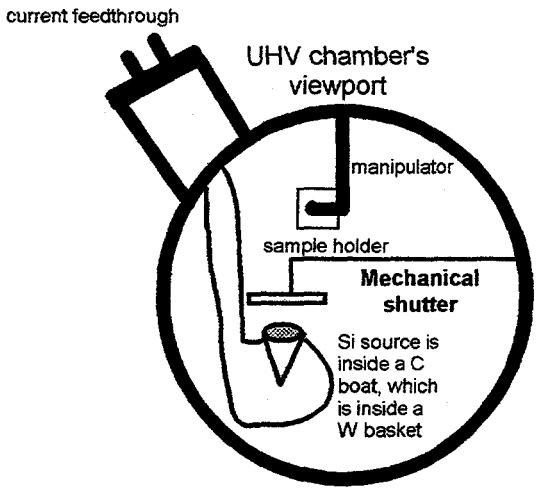

Figure 2.9a A schematic diagram of the gas aggregation deposition set up for the synthesis of Si nanoclusters.

The details of nucleation and cluster formation can be understood as following:

<u>* Homogeneous nucleation:</u>

This is the case when a liquid or solid is evaporated at a high vapor pressure in an UHV environment. The elevation of the Gibbs free energy required to form a spherical embryo with g molecules is:[37]

$$\Delta G = 4\pi r^2 \sigma + g(\mu_r - \mu) \qquad (30)$$

where μ_r is the chemical potential of an atom (or molecule) in the spherical embryo (or condensed phase), μ is the chemical potential of an atom (or molecule)

in the vapor phase, and σ is the surface free energy per unit area of the spherical embryo (also called nucleus, drop, grain, or cluster). In this equation, the first term on the right hand side represents the increase in surface free energy from 0 to $4\pi r^2\sigma$ as the embryo is formed from the vapor phase. The second term on the right hand side represents the change in chemical potential between an atom in the embryo (condensed phase) and an atom in the vapor phase.

Here: $\mu_r - \mu = -kT\ln(\frac{p_r}{p_\infty})$,[38,39] where p_∞ is the equilibrium vapor pressure at temperature T of a plane bulk surface, p_r is the vapor pressure of a spherical embryo of radius r, and k is the Boltzmann constant. It is noted that $\frac{p_r}{p_\infty} > 1$ since the surface to volume ratio of a spherical embryo is greater than that of a plane bulk surface. Conventionally, p_r is taken to be the same as the actually measured ambient vapor pressure, which is also called the supersaturation vapor pressure. Equation [30] can then be rewritten as:

$$\Delta\dot{G} = \sigma\ 4\pi\ r^2 - gkT\ln(\frac{p_r}{p_\infty})$$

$$= \sigma\ 4\pi\ r^2 - \frac{4}{3}\pi\ r^3 nkT\ln(\frac{p_r}{p_\infty}) \qquad (31)$$

where n is the number of atoms (or molecules) per unit volume of the embryo.

This expression exhibits a maximum at a certain critical size r^* when $\frac{\partial(\Delta G)}{\partial r}^{set} = 0$,

$$\text{or } r^* = \frac{2\sigma}{nkT\ln(\frac{p_r}{p_\infty})} \tag{32}$$

Figure 2.9b shows a plot of ΔG as a function of the embryo radius r for a supersaturation ratio $\frac{p_r}{p_\infty} > 1$, adapted from reference [38].

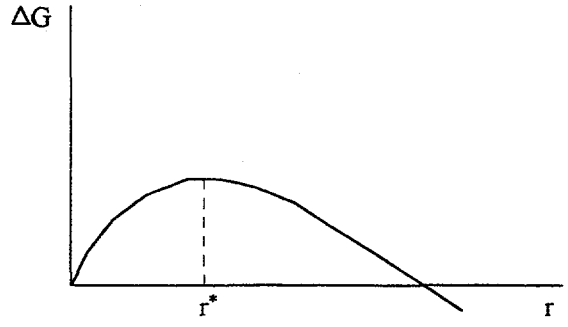

Figure 2.9b A plot of the free energy ΔG as a function of the embryo radius r for a supersaturation ratio $\frac{p_r}{p_\infty} > 1$, adapted from reference [38].

From figure 2.9b, it is observed that the critical radius r^* corresponds to an unstable equilibrium. ΔG decreases on both sides of the critical radius r^*. So, embryos with radii larger than r^* tend to grow larger while embryos with radii smaller than r^* tend to evaporate.

* Heterogenous nucleation:

This is the case of nucleation in the presence of a colder inert buffer gas such as Ar. The colder inert buffer gas cools the evaporated atoms, molecules, clusters and lower their kinetic energy. A stabilizing three body collision can occur similar to the following equation:

$$Si + Si + Ar \rightarrow Si_2 + Ar \qquad (33)$$

This dimer formation starts the condensation process if dimers or larger aggregates are not already present in the gas prior to expansion.[36]

In this process, the Ar atoms pick up energy through collisional formation of Si clusters which act as condensation nuclei for further growth. If the ratio of monomers to clusters is great, the latter grow by monomer addition. For heavily clustered beams, cluster-cluster aggregation becomes important.

Cluster growth laws for a simpler system of precipitation from supersaturated solid solutions have been formulated by Lifshitz and Slezov.[40,41]

Lifshitz-Slezov's asymptotic cluster growth law is found to be a direct consequence of the rate with which monomers from the surrounding medium arrive at the cluster surface. The rate equation for the number of monomers N in a cluster is written as:

$$\frac{dN}{dt} = g_N - l_N \qquad (34)$$

where g_N and l_N are the rate at which mononers from surrounding condense into the cluster, and the rate at which monomers from the cluster escape to the surrounding by thermionic emission. Equation [34] can be rewritten as:

$$\frac{dR}{dt} = \frac{v}{n_o}[n_v(R) - n_T(R)] \tag{35}$$

With $l_N = v\ An_T(R)$, $g_N = v\ An_v(R)$, and $N = \frac{4}{3}\pi\ n_o R^3$

where v is the monomer thermal velocity, $A = 4\pi\ R^2$ is the surface area of a spherical cluster of radius R, n_o is the monomer density inside the cluster, $n_v(R)$ is the monomer density just outside the surface of a cluster of radius R, and $n_T(R)$ is the monomer thermal density just inside the cluster surface. Here, it is noted that $n_T(R) \propto \exp(-\phi / T)\exp(\sigma / R)$, where ϕ is the volume energy, T is the temperature, and the factor $\exp(\sigma / R)$ is a surface contribution term with σ proportional to the surface tension of the cluster. Assuming that monomers diffuse through the surrounding medium, that the total number of monomers are conserved, and using many mathematical transformations, Lifshitz and Slezov derived at the following growth law for the average cluster radius:[40,41]

$$\overline{R}^3(t) - \overline{R}_o^{\,3} = B(t - t_o) \tag{36}$$

where $\overline{R}_o$ is the initial average particle size (or the critical radius of the precipitates) before coarsening begins, t_o is the time at which coarsening begins, and B is some rate constant.

From equation [36], it can be said that the mean cluster radius increases with travel time or equivalently travel distance.

*Gas aggregation method:

The results of equation [32] and [36] can be applied qualitatively to the clusters synthesized by the technique of gas aggregation method. However, the quantitative detail of the process is rather complicated and not well studied, due to the interdependence of many parameters involved such as the temperature of the source, the buffer gas pressure, and the source to substrate distance. There are marked temperature and monomer density gradients between the source and the substrate in the gas aggregation technique, which are not present in the case of precipitation from supersaturated solid solution. In addition, complication that arises from the convection effect in the gas aggregation method cannot be ignored. No scaling law exists.[36]

In this technique, the mean cluster radius increases not only with the source to substrate distance, and the source temperature, but also with the inert buffer gas pressure. As the buffer gas pressure is increased, the expansion of vapor is more strongly suppressed. This leads to bigger clusters with a lower density (of clusters). Cluster growth stops, nevertheless, at some finite vertical distance from the evaporating boat because of a rapid drop in temperature and vapor pressure away from the boat. The inert buffer gas also serves to cool down the clusters by

convection. A picture of gas candle-flame like smoke of silver clusters arising from heating silver to 1400 °C in a buffer of He at 50 Torr is shown in figure 2.9c, taken from reference [42]. The arrows in the picture indicate the direction of the convection flow.

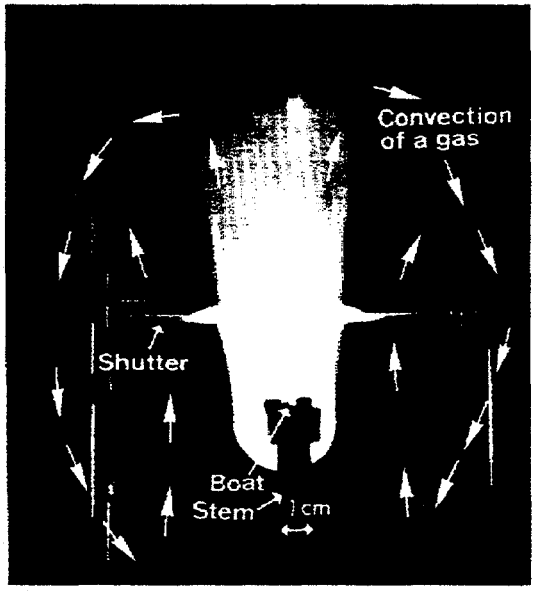

Figure 2.9c Candle-flame like smoke of silver clusters arising from heating silver to 1400 °C in a buffer of He at 50 Torr, taken from reference [42].

2.9a Production of surface passivated Si nanoclusters

To produce H passivated nc-Si, the Ar buffer gas was pumped out of the synthesis chamber after the deposition of roughly one layer of nc-Si (as observed by STM). The sample was then exposed to atomic hydrogen by passing molecular hydrogen at 2 x 10^{-6} Torr through a very fine tungsten mesh at 2000 °C. The sample to tungsten mesh distance was about 3-5cm. This is a well known

technique to passivate Si wafers with hydrogen.[43,44] After 5 minutes of exposure and a subsequent removal of hydrogen, Ar was reintroduced into the synthesis chamber. Then, roughly another monolayer of nc-Si was deposited, and the process was repeated until a thick film was formed.

To produce oxygen passivated nc-Si, the procedure was similar to the case of hydrogen passivated nc-Si, except that molecular oxygen at 300 mTorr and room temperature was used instead of atomic hydrogen. After the desired film thickness was reached, the sample was resistively heated in 4×10^{-4} Torr of oxygen to some predetermined temperatures (between 500-800 °C).

2.9b Production of silicon oxide nanostructures.

To produce silicon oxide nanostructures, the synthesis chamber was filled with oxygen (instead of Ar) up to several mTorr prior to Si deposition.

3. RESULT AND DISCUSSION

3.1 Properties of Si nanoclusters synthesized by pulsed laser deposition

The initial method for cluster synthesis was pulsed laser deposition in UHV condition. In this experiment, the chosen substrate was the basal plane of graphite, which is inert since all the carbon bonds in this plane are satisfied. In addition, the well-known structure of the graphite rings on these surfaces can be used as a calibration for subsequent STM images of the clusters. An STM image of a clean graphite surface, obtained from this experiment, is shown in figure 3.1 below:

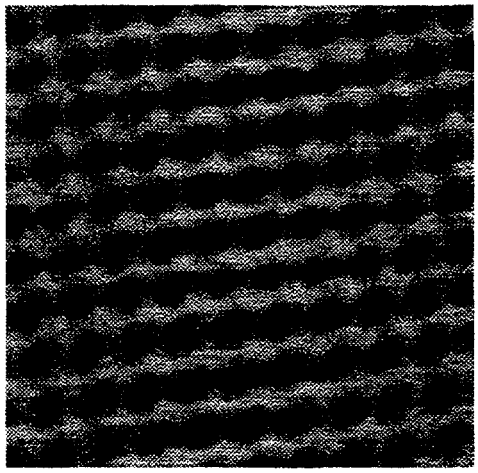

Figure 3.1 An STM image of a clean graphite surface.

Actually, the graphite form of the element carbon consists of a stack of parallel hexagonal net planes, the nearest neighbor atomic spacing in the net planes (or

basal planes) being 1.42×10^{-8} cm and the spacing between net planes 3.35×10^{-8} cm. The planar stacking sequence found in graphite is either ABABA .... (hexagonal lattice) or ABCABC .... (rhombohedral lattice). Obviously, the graphite rings obtained from STM do not look hexagonal at all. In fact, they look more like parallelograms with interatomic distance of about 2.45×10^{-8} cm. This STM image is a product of the planar stacking sequences of graphite and the nature of the STM tunneling current. Due to the exponential dependence of the STM current on the tunneling distance, probably only electrons from atoms in the first two adjacent net planes would contribute significantly to the experimentally measured tunneling current. The basal plane projection of the first two adjacent planes of graphite is shown in figure 3.2.

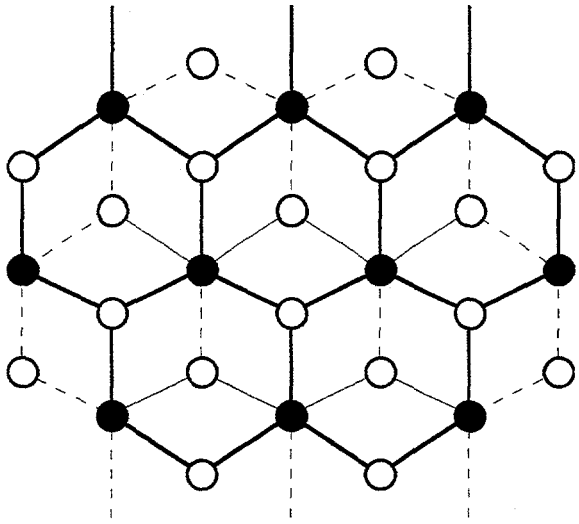

Figure 3.2 Basal plane projection of the first two adjacent planes of graphite.

In this figure, the black circles represent positions where atoms in the first plane sit right on top of atoms in the second plane. At these positions the STM tunneling current is more intensified. And as a result, the STM image of the basal plane of graphite seems to consists of parallelograms.

In figure 3.3, curve (a) shows an Auger spectrum of the as-deposited Si on graphite. The peak near 270 eV was from the carbon KLL Auger transition. The peak near 90 eV was from the Si LMM Auger transition. Less than 1% of the surface was covered by adsorbed oxygen which is seen near 500 eV. Curve (b) shows the Auger spectrum of the same sample after annealing to 500 °C for 5 minutes. Here a reduction in the Si Auger peak is observed. A reduction in this Auger peak is consistent with a reduction in the surface area covered by Si, which through surface diffusion formed bigger clusters.

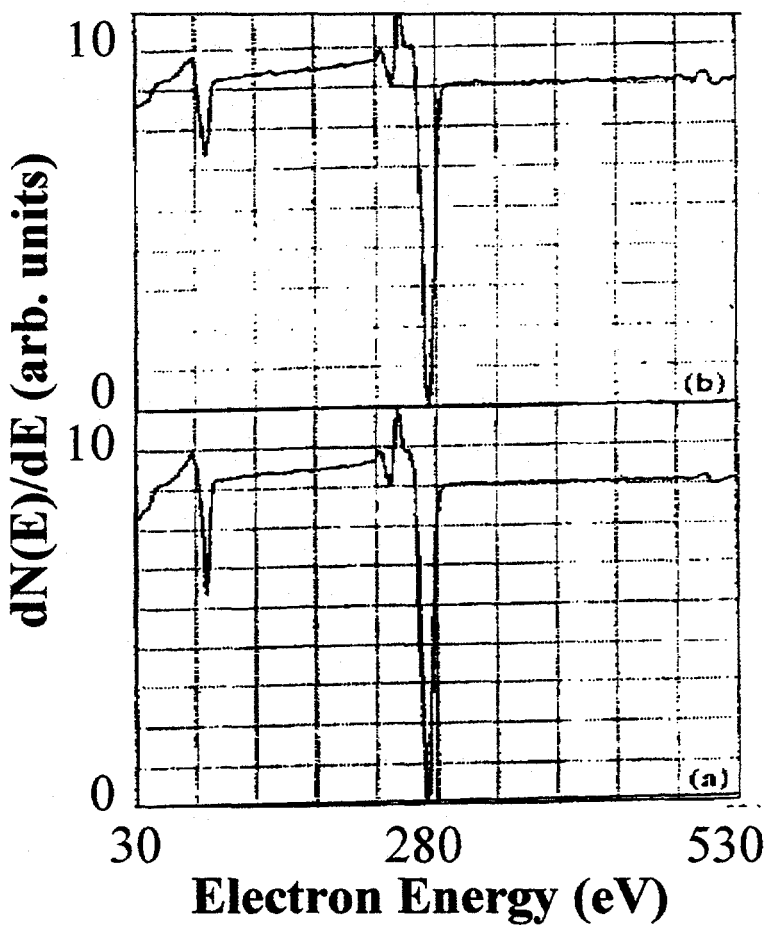

Figure 3.3 Auger electron spectra of (a) as-deposited Si on HOPG; (b) the same sample after annealing to 500 °C for 5 minutes.

Figure 3.4 shows an STM image of Si clusters formed on graphite after substrate annealing to 500 °C for 5 minutes. A tendency to form aggregations of Si atoms of average size of 3.0 nm in diameter with a FWHM of about 2nm can be observed, even though the as-deposited Si had no definite shape or size.

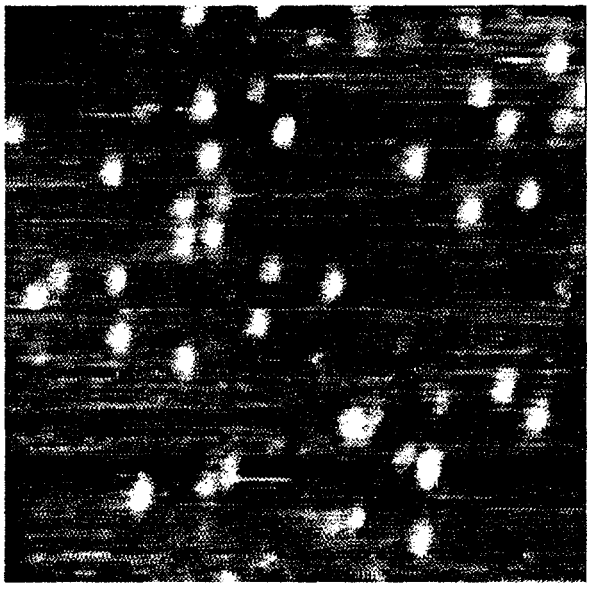

Figure 3.4 STM image of Si clusters formed on HOPG after substrate annealing to 500 °C for 5 minutes.

The size distribution of the annealed clusters from the same sample is shown in figure 3.5. The size distribution in this technique depends on the temperature, the annealing time, as well as the amount of materials initially deposited on the substrate surface (usually, one to a few monolayers). Clustering behaviors are probably dependent on substrate materials too.

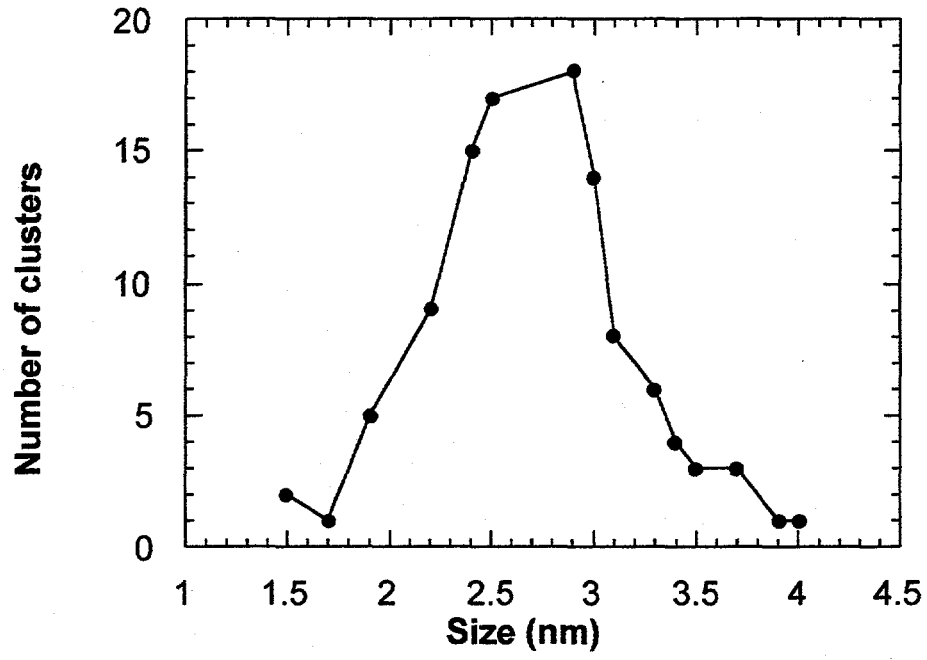

Figure 3.5 Cluster size distribution of a sample with an average cluster size of 3.0 nm in diameter and a FWHM of 2 nm after annealing to 500 °C for 5 minutes.

As the substrate temperature was raised to 800 °C, a surface wetting (SiC interface formation) was evidenced by an increase in the Si Auger peak (hence an increase in the surface area covered by Si) as shown in figure 3.6. This surface wetting was probably the result of the reaction of Si with thermally broken π bonds in the graphite rings.

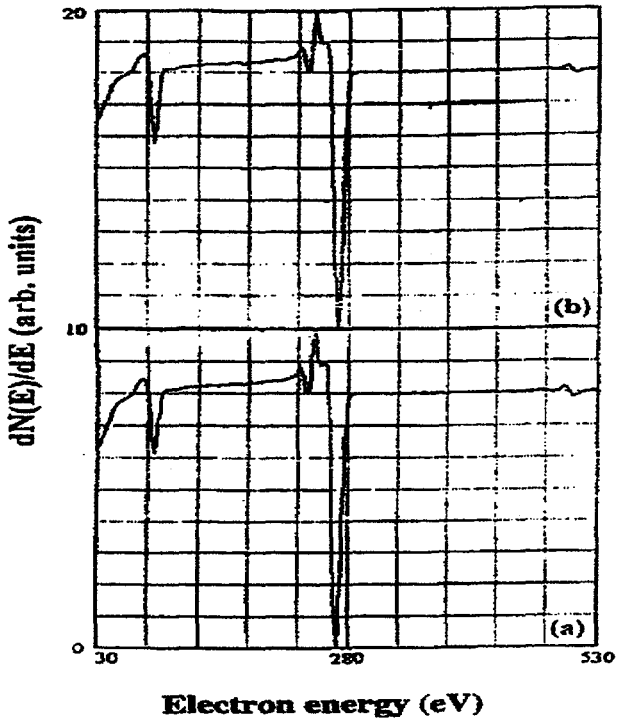

Figure 3.6 Auger electron spectra of (a) as-deposited Si on HOPG; (b) the same sample after annealing to 800 °C for 5 minutes.

Since this wetting complicated the interpretation of the optical spectra obtained from Si nanoclusters on HOPG, none of the samples reported hereafter was heated to more than 600 °C. No detectable PL from the as-deposited clusters was observed in the wavelength range of 400-900 nm. This behavior was expected from a surface with dangling bonds and/or surface reconstruction. In this case, surface states are known to exist in the forbidden gap and to quench the PL.[22,23] Passivation of the dangling bonds is necessary if these clusters are to be of any use

in optical applications. To passivate the surface dangling bonds, many samples were exposed to atomic hydrogen, which is substantially more reactive with Si than molecular hydrogen, by passing molecular hydrogen at 2 x 10^{-6} Torr through a very fine tungsten mesh at 2000 °C. The sample to tungsten mesh distance was about 3 cm. That did not result in any detectable visible photoluminescence from the clusters.

For many other samples which had not been exposed to hydrogen, surface passivation was carried out by flowing oxygen at up to 10^{-6} Torr into the UHV chamber for up to 8 hours. Auger spectra show adsorption of oxygen on the surface of the clusters without Si oxide formation. This was evidenced by a lack of Si LMM Auger peak shift from 92 eV toward lower energy (about 60 eV for SiO_2 and 80 eV for partially oxidized Si). Again, no visible photoluminescence was detected. Moreover, experiments in which the clusters had been annealed to 500 °C in 10^{-6} Torr of O_2 for 5 minutes, then exposed to O_2 at up to 300 mTorr for five days also resulted in clusters with no detectable visible PL. Subsequent *in situ* heating of the oxidized samples up to 600 °C for 10 minutes at 10^{-6} Torr of oxygen did not help the PL either. Thus the presumably passivated Si clusters did not emit the deep red band characteristic of porous Si, although the possibility that this was caused by nonradiative decay of excitation in the Si cores to the graphite substrate cannot be ruled out. The samples were then removed from the UHV chamber and

exposed to ambient air for more than four months. This resulted in strong red to green-blue PL spectra (figure 3.7). These spectra remained stable after hours of continuous illumination by the He-Cd laser beam, and even after heat treatment up to 450 °C in the UHV chamber.

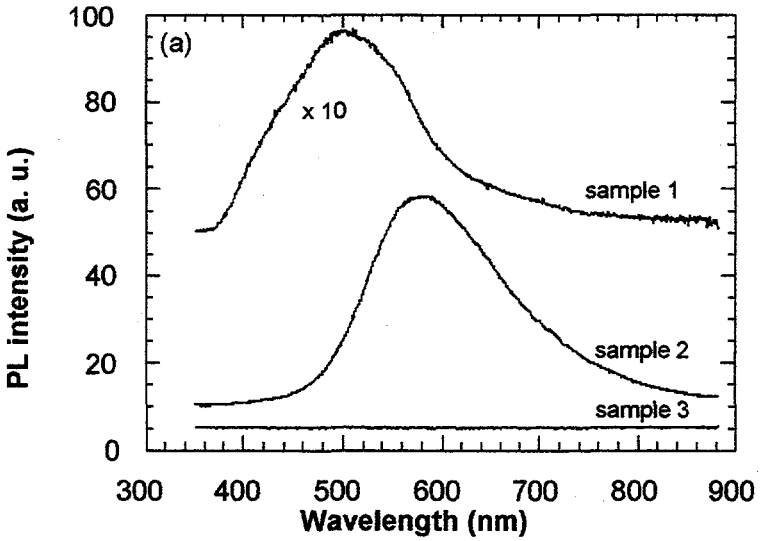

Figure 3.7 PL spectra of oxidized Si clusters. Sample 1 and sample 2 contained clusters with average diameter, before oxidation, of 3 and 5 nm respectively. Both were exposed to air for more than four months. Sample 3 was oxidized in the synthesis chamber for five days at 300 mTorr of O_2 and had no detectable visible PL.

Further study of the prolonged air-exposed samples and the 300 mTorr *in situ* oxidized samples by x-ray photoelectron spectroscopy (XPS) with a Mg Kα x-rays (1253.6 eV) source, revealed the existence of only SiO_2 for the prolonged air

exposed samples, and the existence of SiO_X (x ranged from 0 to 2) for the *in situ* oxidized samples, (figure 3.8).

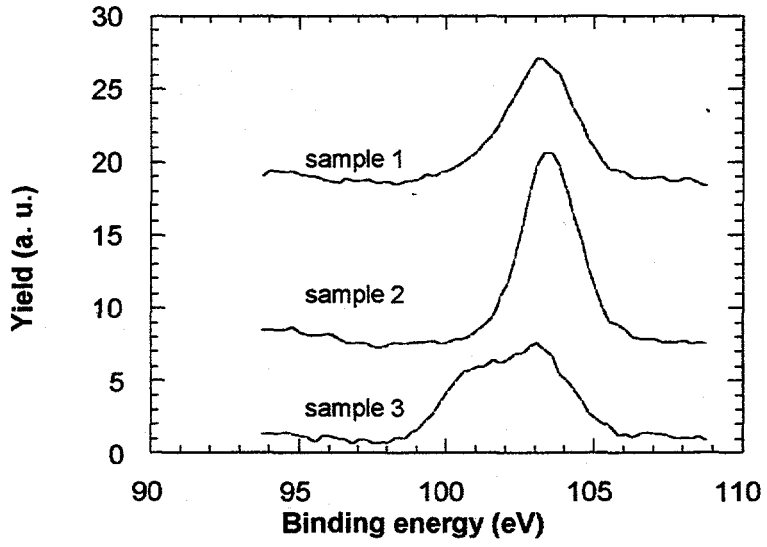

Figure 3.8 X-ray photoelectron spectra of the corresponding clusters in figure 3.7.

This result is not surprising, since time is needed to grow a thick Si oxide layer and moisture in air is known to speed up the oxidation process.[45] In figure 3.8, the peak near 99.5 eV binding energy is due to photoelectrons from Si 2P core-level transition. This peak is shifted to 103.5 eV for SiO_2. Smaller shifts are expected for intermediate oxidation states of Si in SiO_X.[46] The size of the Si cores that could be remaining in the oxidized clusters was estimated from the XPS data. The clusters were taken to be perfect spheres, and correction for the volume

difference between Si and SiO_2 was considered. The detection limit was assumed to be such that the ratio of the signal contributed from the unoxidized Si cores (S_1) to that contributed from the Si oxide outer layer, taken as SiO_2 (S_2) must be greater than the experimentally measured noise to signal ratio, N/S from the XPS spectra,

$$\text{i.e., } \frac{S_1}{S_2} > \frac{N}{S} \tag{37}$$

with

$$S_1 \propto \int_0^{R_i} 4\pi\, r^2 e^{-(R_o - r)/l} dr \tag{38}$$

$$S_2 \propto \int_{R_i}^{R_o} 4\pi\, r^2 e^{-(R_o - r)/l} dr \tag{39}$$

In the above formula, R_i is the average radius of the unoxidized Si cores; R_o is the average radius of the clusters (consisting of Si oxide outer layers and unoxidized Si cores); and l=3.8 nm is the escape depth for electrons with kinetic energy of about 1150 eV.[47] With an experimental N/S ratio of about 3.3%, unoxidized Si cores with average radius >0.6 nm (1.05 nm) from clusters with average radius of 1.5 nm (2.5 nm) before oxidation were within the detection limit.

Next, the samples were dipped into a 20 % HF solution for 20 seconds, then in de-ionized water for 3s, and reexamined in the UHV chamber. HF treatment is known to effectively etch away the silicon oxide layer, and passivate the Si inner cores with hydrogen.[43,44,48] This HF treatment stripped away all or most of the oxide layer from the clusters and allowed the detection of any unoxidized Si cores.

Figure 3.9 shows the Auger electron spectra (AES) of pure graphite (a), and sample 1 before (b) and after HF treatment (c). Clearly, almost all Si oxide has been etched away. The peaks around 272 eV and 503 eV were from carbon and oxygen KLL Auger transition respectively. The Si LMM Auger transition at 92 eV was absent, while the peaks around 60 eV and 80 eV were from oxidized Si.

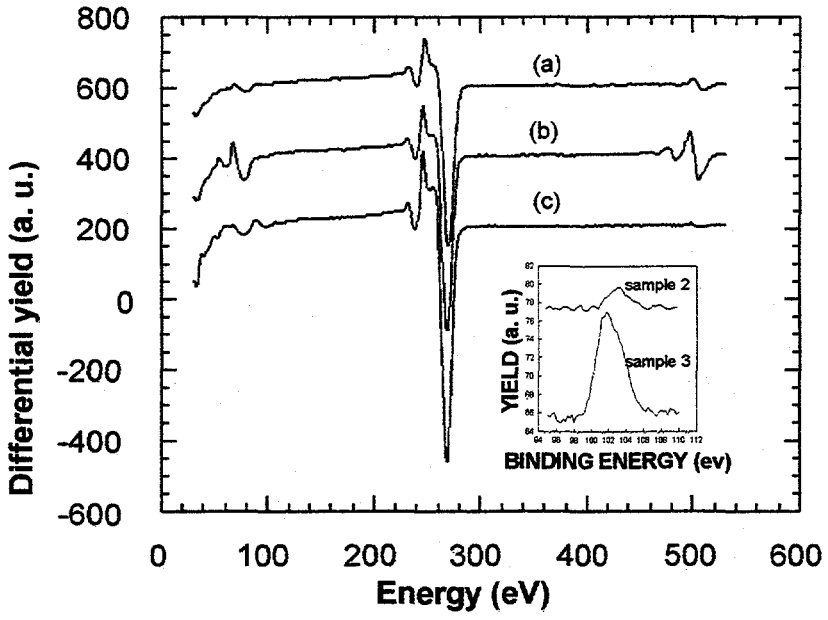

Figure 3.9 Auger electron spectra (AES) of pure graphite (a), and sample 1 before (b) and after HF treatment (c). The inset shows XPS spectra of samples 2 and 3 after HF treatment.

After HF treatment, the XPS spectrum for sample 1, which had an average cluster size of 3 nm in diameter before air exposure, showed no evidence of unoxidized Si. Similar result was found for sample 2, while sample 3 showed evidence of

unoxidized Si before and after HF treatment (inset of figure 3.9). This implies that there were no unoxidized Si cores in the prolonged air exposed samples, and that the observed visible PL originated from localized defects in SiO_2. Defects in SiO_2 are known to have emission bands in the energy range of 2-4 eV,[49-51] which overlaps the energy range of the bands observed for the clusters in figure 3.7. The oxide related luminescence caused by nonbridging oxygen defect centers and other oxide related defects in porous Si (which contains Si nanostructures) has been addressed by Prokes,[50,51] and seems to be in qualitative agreement with the result presented here. Also, in some types of nonbridging oxygen defect centers, the PL intensities and energies are known to vary with OH content.[50,51] The difference in PL wavelengths and intensities in the samples may, therefore, be due to differences in their oxygen content, relative ratios of different types of defect centers involved, and OH content.[52]

In summary, Si nanoclusters have been synthesized on the basal plane of HOPG, by laser ablation of Si onto HOPG substrates, followed by annealing of the substrates. The size distribution and shape of the clusters were determined as a function of the annealing time, temperature, and amount of Si initially deposited. Surface passivation of these clusters with hydrogen and/or oxygen did not result in any detectable visible PL properties, although the possibility of nonradiative decay of excitation in the Si cores to the graphite substrate cannot be ruled out. But

prolonged ambient air exposure of these clusters produced strong and stable red to green-blue PL, which can be attributed to localized defects in the oxidized clusters.

3.2 STS of Si nanoclusters deposited on HOPG

The technique of STS was employed in an attempt to obtain the electronic local density of states (ELDS) of Si nanoclusters on HOPG as a function of sizes. As a calibration, the ELDS of a smooth HOPG substrate was obtained and is shown in figure 3.10. The calculated electronic density of states (EDS) for HOPG obtained from reference [53] is shown in figure 3.11.

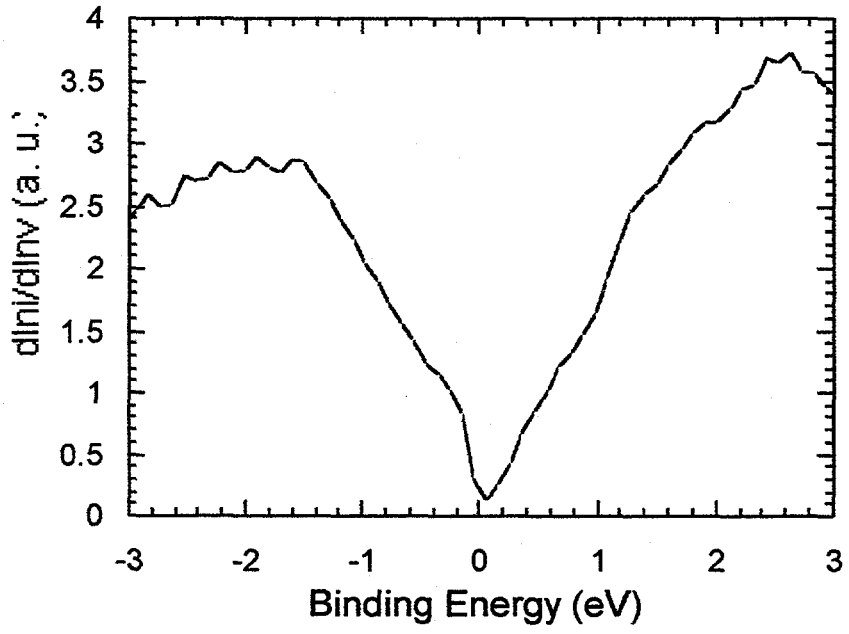

Figure 3.10 STS spectrum of a clean HOPG surface.

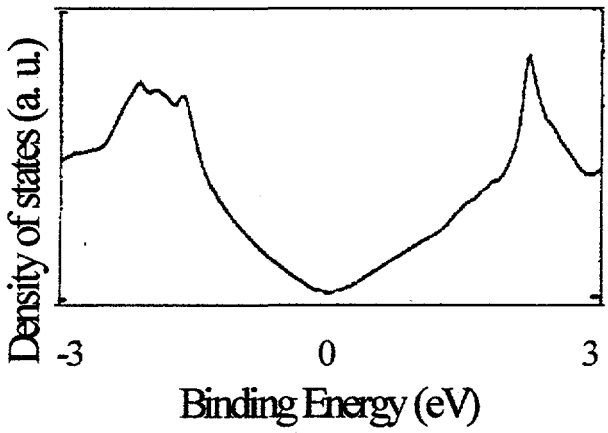

Figure 3.11 The calculated EDS for HOPG obtained from reference [53].

The calculated EDS for the π and π^* bands of graphite shows strong peaks at ~ 2.15 eV (above the Fermi level), -1.5 eV, -1.8 eV and -2.0 eV (below the Fermi level).[53,54,55] Weaker features are also found at ~ 0.75 eV and 1.5 eV. Many of these features are present in the STS spectrum in figure 3.10, although with some energy shifts in the peak positions. An additional peak at ~ -0.35 eV is also noted in the STS spectrum. The discrepancy between the calculated EDS and the STS spectrum is probably caused by surface local states. The calculated EDS is for bulk graphite, while the STS spectrum is more surface sensitive and therefore may pick up surface local states. This STS curve was obtained by first imaging over a graphite surface at a bias voltage of about -210 mV and a

tunneling current of about 0.6 nA. When an atomic resolution STM image of the graphite surface was observed from a 2.5 nm x 2.5 nm scan, the microscope was immediately switched to STS mode (with constant height). The main features (the peak at ~2.2 to 2.4 eV, -1.5 eV to -2.0 eV) in this STS curve for graphite were easily reproduced from sample to sample, provided they were all outgassed by heat treatment to at least 400 °C and atomically smooth.

However, when the technique of STS was applied on any Si nanocluster on a graphite substrate, STS spectra were noisy, nonreproducible, and therefore are not presented here. This was probably due to the lack of a good electrical contact between the graphite substrate and the Si nanocluster under study. Since the synthesized Si nanoclusters sat on the graphite substrate by just Van der Waals and electrostatic forces, they may have been sloshed around by the voltage ramp (from -3V to 3 V) during the STS cycle, causing bad STS spectra. In fact, the easy mobility of the synthesized Si nanoclusters on graphite substrates can be seen in figures 3-12 and 3-13.

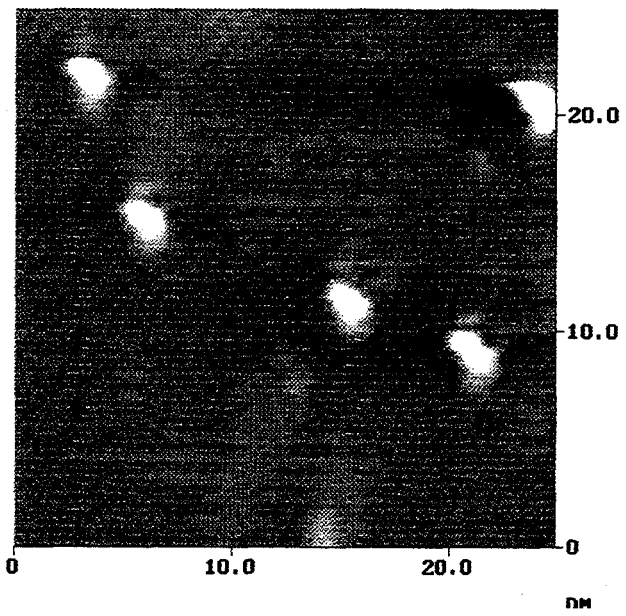

Figure 3.12 STM image of some Si nanoclusters on graphite.

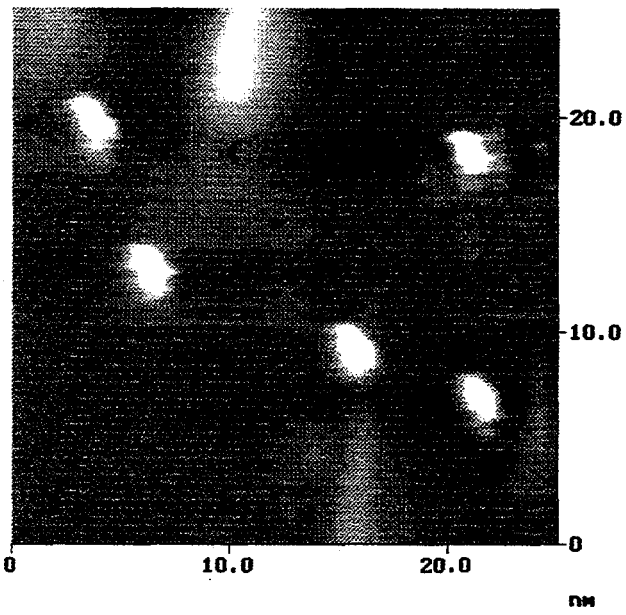

Figure 3.13 STM induced movement of Si nanoclusters on graphite.

In these STM pictures, which were taken about 1 minute apart, note the changing positions of the clusters labeled A, B, and C. These clusters were probably moved around by the STM tip during the scan. Thus, it is reasonable to conclude that the technique of STS is not readily suitable for investigating ELDS of clusters that stick to a substrate just by Van der Waals and/or electrostatic forces.

3.3 Properties of Si nanoclusters synthesized by pulsed laser deposition in an Ar gas

The synthesis of Si nanoclusters by laser ablation followed by substrate annealing, is limited to the production of only less than one layer of clusters. In order to get strong optical signals from the Si nanoclusters, a film consisting of multilayers of Si nanoclusters with a thickness comparable to the absorption length of light is more desirable. The technique of multi-shot laser ablation of a Si target in an inert buffer gas may be the solution to the problem. This is because the nucleation and growth of clusters in this technique happen during the flight away from the Si target, before Si reaches the substrate.

Figure 3.14 and 3.15 show the STM and optical images of a small area and a large area of a same Si film deposited by laser ablation in Ar at about 250 mTorr.

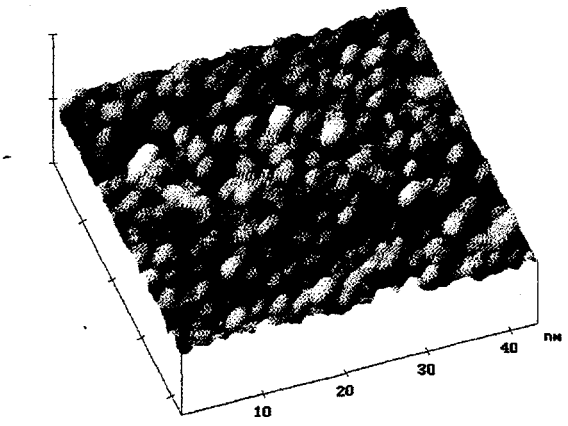

Figure 3-14 STM image of a small area of a Si film deposited by laser ablation in Ar at about 250 mTorr.

Fairly uniform clusters of about 3 nm were observed in figure 3.14. Nonetheless, the existence of micrometer size Si particulates was clearly seen when a bigger area of the film was studied, as in figure 3.15.

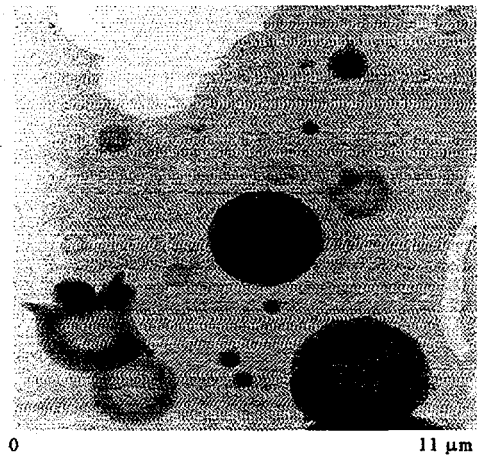

Figure 3.15 Optical image of a large area of a Si film deposited by laser ablation in Ar at about 250 mTorr.

So, pulsed laser deposition in an inert buffer gas can produce Si films consisting of multilayer of Si clusters, with a very wide size distribution ranging from a few nanometer to many micrometers. As described in the chapter on experimental procedure, Si nanoclusters are formed by coalescence of Si atoms from the vapor species during their flight from the target to the substrate. On the other hand, the micrometer size particulates are formed by hydrodynamic and/or exfoliational sputtering of the Si target. However, from the fairly round shape observed from most of the micrometer size particulates, it is more probable that they were originally liquid dropplets formed by hydrodynamic sputtering. During the flight away from the ablated target, Si clusters suffer many collisions with the Ar buffer gas. As a result, many Si atoms and small clusters experience significant changes in flight directions, and never make their way to the substrate, while some others may zig-zag their way to the substrate. In contrast to the small clusters, the micrometer particulates (or microclusters) are expected to be affected much less by collisions with the Ar buffer gas. Their initial flight direction should remain unchanged.

Based on the above analysis, an experimental trick aimed at eliminating the microclusters was carried out as illustrated in figure 3.16. In this setup, the substrate was rotated almost 90 ° away from the ablated target. In such a geometry, the micrometer particulates would miss the substrate while much smaller clusters

may make their way to the substrate, through changes in their flight directions upon collision with the buffer gas.

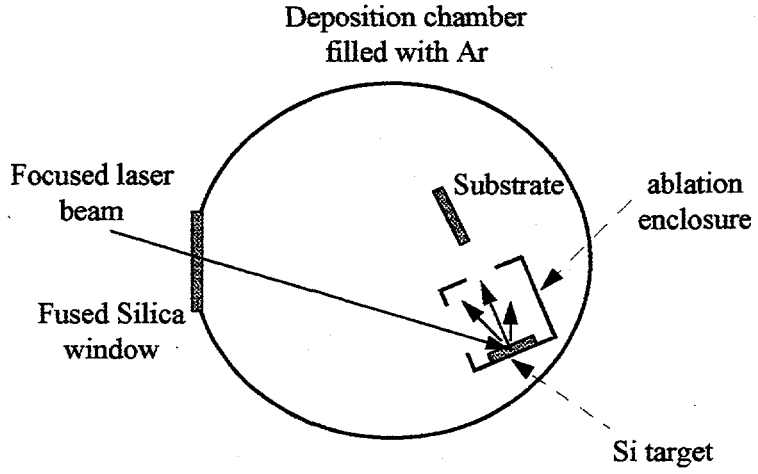

Figure 3.16 A pulsed laser deposition setup which reduces the number of micrometer size Si flakes or particulates.

Experimental results from this setup show that although a complete removal of micrometer particulates was not achieved, a significant reduction of these particulates in the deposited film was observed. However, the deposition efficiency in this technique, suffers dramatically since the substrate surface area normal to the Si target is significantly reduced.

In order to make a multilayer film of Si nanoclusters with a narrow size distribution, pulsed laser deposition techniques were abandoned from this point on in favor of a different deposition technique: gas aggregation method.

3.4 Properties of Si nanoclusters deposited by the gas aggregation method

3.4a Surface passivated Si nanocrystals (nc-Si)

1. Size, composition and crystallinity

The inset of figure 3.17 shows a constant current STM image of approximately one monolayer of Si clusters, with average diameters of 5 nm before oxidation, deposited on HOPG substrate by vaporization of Si at 1700 °C in an Ar buffer gas of 500 mTorr, and at a source to substrate distance of 5.0 cm.

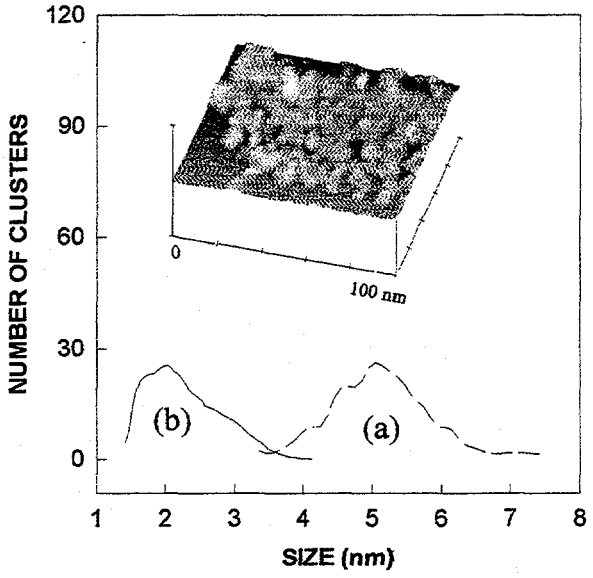

Figure 3-17 Size distributions of the Si cores of a sample deposited on HOPG substrate by vaporization of Si at 1700 °C in an Ar buffer gas of 500 mTorr, and at a source to substrate distance of 5.0 cm, (a) before oxygen passivation, and (b) after oxygen passivation. The inset shows an STM image of roughly one layer of such Si clusters before oxygen passivation.

Curve 1(a) shows the distribution of diameters determined by STM[57] from a collection of 300 Si clusters of the same sample. The actual STM image is shown in the inset of figure 3.17. An average diameter of about 5 nm and a full width at half maximum (FWHM) of about 2 nm is observed. Curve 1(b) shows a distribution of the diameters of the Si cores of 250 Si clusters from the same sample as in the inset obtained from HRTEM measurements after a surface oxide layer has formed during oxidation in dry oxygen up to 800 °C for 5 minutes. The sharp cut off at small nanocluster size is an artifact due to the difficulty of the employed HRTEM in reliably detecting clusters smaller than 1 nm in diameter. The average size of these cluster cores is approximately 2 nm, so the thickness of the silicon oxide layer on these nanocrystals is about 1.5 nm. Other samples with average as-deposited (before oxidation) cluster size in the range of 3.5-6.5 nm also have size distributions with FWHM of about 2.0 ± 0.2 nm, and silicon oxide outer layers with thickness of about 1.2-1.5 nm.

The composition of the as-deposited Si nanoclusters during synthesis was monitored by (AES). In figure 3.18, curve (a) shows the AES spectrum from the degassed HOPG substrate. The dip around 272 eV is the C(KLL) Auger transition from the HOPG substrate. A small dip at about 92 eV due to the Si(LMM) Auger transition was observed after the deposition of roughly one layer of Si clusters (curve (b)). Note that there was no observable oxygen contamination. But after 5

minutes of exposure to 300 mTorr of molecular oxygen, a small dip at about 503 eV due to the O(KLL) Auger transition was present (curve (c)). The above process was continued one layer of clusters at a time until a thick film of surface oxidized Si nanoclusters was obtained (curve (d)). The dips near 60 eV and 80 eV are signatures of SiO_2 and SiO_x ($0 < x \leq 2$) respectively.

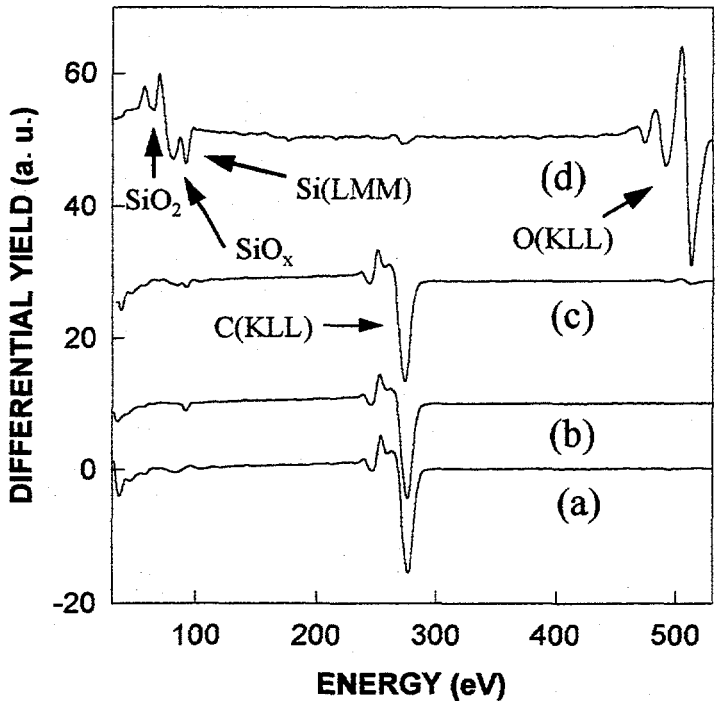

Figure 3-18 (a) AES spectra of a clean HOPG surface, (b) with roughly one layer of Si nanocrystals before any oxygen exposure, (c) after exposure to 300 mTorr of oxygen at room temperature, and (d) after the formation of a thick film of oxygen passivated nanocrystals.

HRTEM and XRD revealed that Si nanoclusters synthesized by this technique had the cubic crystalline structure of bulk silicon. Figure 3.19 shows an XRD plot of a sample of Si nanoclusters deposited on a glass slide by vaporization of Si at 1900 °C in an Ar pressure of 3000 mTorr, and at a source to substrate distance of 6.5 cm. This sample was a film of about 10 μm thick of initially unpassivated nanocrystals, and was exposed to air for 2 days prior to XRD measurement.

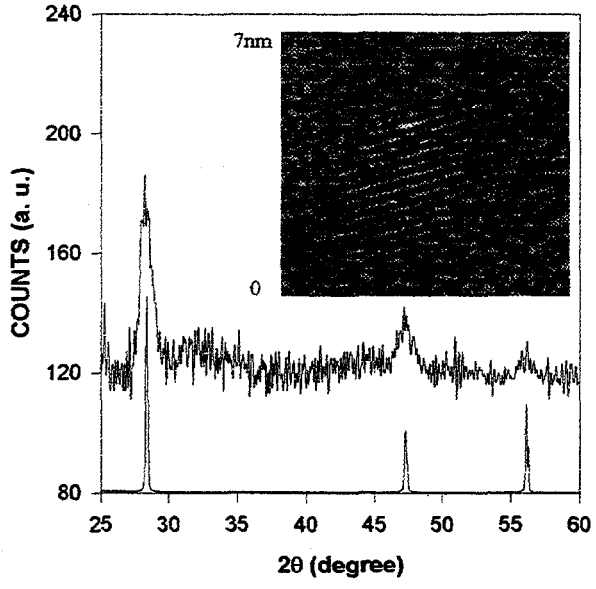

Figure 3-19 XRD of large grain Si microcrystals (bottom curve), and of Si nanocrystals deposited on a glass slide by vaporization of Si at 1900 °C in an Ar pressure of 3000 mTorr, and a source to substrate distance of 6.5 cm (upper curve). The inset shows HRTEM image of a Si nanocrystallite in an amorphous SiO_x matrix on an amorphous carbon coated Cu HRTEM grid. This sample was synthesized by vaporization of Si at 1700 °C in an Ar pressure of 2000 mTorr, and a source to substrate distance of 5 cm.

In figure 3.19, the lower curve shows Si diffraction peaks from the (111), (220), and (311) planes of a calibration sample of microcrystalline Si powder with grain sizes > 10 μm. All of the allowed diffraction peaks from the calibration sample were present in the sample of silicon nanocrystals. The diffraction peaks of the nanocrystalline film are broadened due to the small size of the crystals. From the Scherrer formula[27] and the width of the diffraction peaks, the average diameter of nc-Si was determined to be 8 nm for this sample. Strain and stress on these nc-Si could contribute to the observed broadening.[58] This effect was probably small, however, because there was reasonable agreement between the XRD and HRTEM measurements on similar samples. The inset of figure 3 shows an HRTEM image of a Si nanocrystallite from a sample deposited on a Mo substrate by vaporization of Si at 1700 °C, in an Ar pressure of 2000 mTorr, and at a source to substrate distance of 5 cm. This sample was not passivated, and was air exposed for 2 days prior to HRTEM measurement. As can be seen in the inset, Si lattice fringes, from (111) planes with lattice spacing of about 0.3134 nm, were clearly observed in a background of amorphous Si oxide, on the amorphous carbon coated Cu HRTEM grid. This particular Si nanocrystallite had a Si core of about 4.7 nm in diameter, which was also the average size for the film. It was also observed from HRTEM that the oxide layers covering the Si cores from all of the samples varied between 1.2 to 1.5 nm whether they were air exposed for 2 days or 2 weeks. This result was

also true for samples subjected to annealing to 800°C for 5 minutes in dry oxygen of about 4×10^{-4} Torr. So, in general, the synthesized Si clusters were nc-Si, the surfaces of which were either terminated with hydrogen, or, if passivated with oxygen, they were covered with 1.2-1.5 nm thick layers of SiO_x ($0 < x \leq 2$). Following is a table summarizing the experimentally measured sizes of Si nanocrystals as a function of Ar pressure, Si source temperature, and source to substrate distance:

Ar Pressure (mTorr)	Source temperature (°C)	Source-sample distance (cm)	Average unoxidized Si core diameter (nm)
250	1700	5	3.5 before oxidation
500	1700	5	5.0 before oxidation
1000	1700	5	6.5 before oxidation
2000	1700	5	4.7 after oxidation
3000	1900	6.5	8.0 after oxidation

Table 1 Measured sizes of Si nanocrystals as a function of Ar pressure, Si source temperature, and source to substrate distance.

2. PL properties

Unpassivated nc-Si did not exhibit any PL detectable by the Si detector in the energy range > 1.2 eV; this is expected due to the quenching effect of the dangling bonds. However, all surface passivated nc-Si showed easily detectable infrared and/or visible PL, the intensity of which depended roughly linearly on the exciting laser beam intensity. It was also observed that excitation by either the 325 nm line

from the He-Cd laser or the 488.8 nm line from the Ar ion laser produced similar PL shape for a given sample.

Figure 3.20 shows PL spectra from hydrogen passivated nc-Si. Curves (a), (b), and (c) correspond to PL from samples made by vaporization of Si at 1700 °C, at a source to substrate distance of 5 cm, and in Ar pressures of 250 mTorr, 500 mTorr, and 1000mTorr respectively.

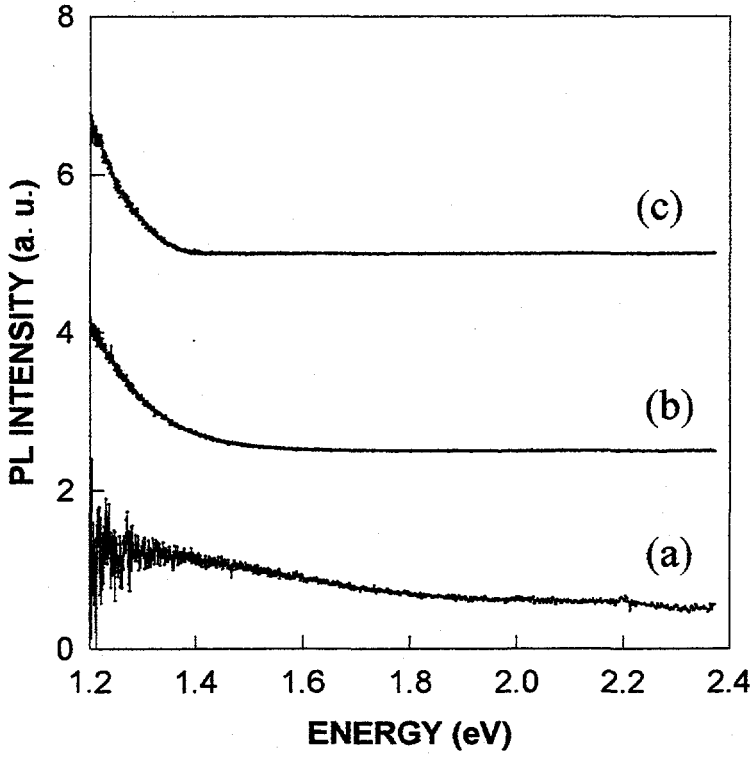

Figure 3-20 PL spectra of hydrogen passivated nc-Si of average diameters of (a) 3.5 nm, (b) 5 nm, and (c) 6.5 nm.

STM measurements of average diameter of these nc-Si yielded average values of 3.5 nm, 5.0 nm, and 6.5 nm for curves (a), (b), and (c) respectively. All three samples exhibited strong near- infrared PL, accompanied by increasing PL intensity at energies below 1.2 eV. A comparison of the relative intensities among the three curves was not possible, since the three samples had different amounts of compactness and film thickness. With decreasing nanocrystal size, however, slight blueshifts were observed for PL edges on the higher energy side of the PL spectra. The increasing PL intensity at photon energies below 1.2 eV is a distinctive characteristic of these hydrogen passivated nanocrystals. This behavior distinguishes them from porous silicon, which has luminescence peaks in the red to the near infrared, accompanied in some cases by additional luminescence peaks below 1.2 eV.[59,60] The increasing PL in many samples at photon energies below ~ 1.2 eV suggests that the surface passivation for these samples is not complete. Optical transitions between states lying in the nc-Si energy gaps are probably responsible for this PL.

Larger PL blueshifts with decreasing nanocrystal size were observed with oxygen passivated nc-Si. This is illustrated in figure 3.21; curves (a), (b), and (c) correspond to PL from samples made by vaporization of Si at 1700°C onto HOPG substrates, at a source to substrate distance of 5 cm, and in an Ar pressure of 500 mTorr, 1000 mTorr, and 2000 mTorr respectively. These samples were exposed to oxygen after each monolayer of nc-Si was deposited, and later annealed in steps

of 150 °C for 5 minutes/step up to 800 °C. Sample (a) had an average nc-Si diameter of 5 nm before oxidation, and average unoxidized Si core diameter of 2 nm after oxidation. This sample exhibited a strong orange-white PL, with PL peak at around 2.2 eV. Sample (b) had an average diameter of 6.5 nm before oxidation, and average unoxidized Si core diameter after oxidation of 3.5 nm. This sample had a bright red PL, with a PL peak at about 1.7 eV and an increase in intensity at lower energies in the infrared. Sample (c) had an average unoxidized Si core diameter of 4.7 nm after oxidation, and exhibited a dark red PL, with PL increasing in the infrared.

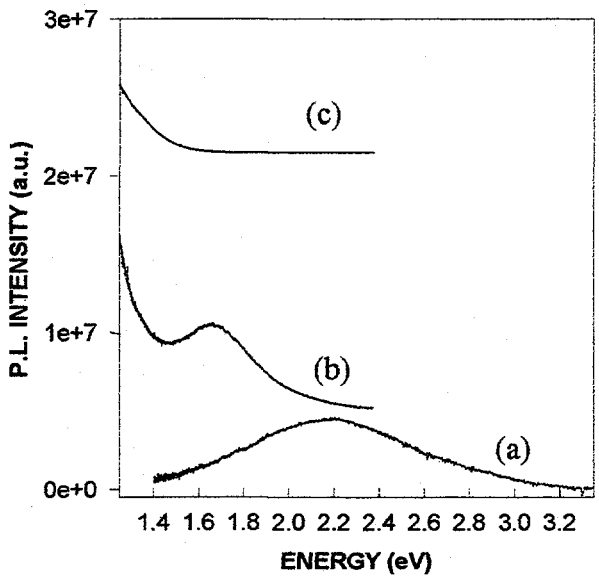

Figure 3.21 PL spectra of oxygen passivated nc-Si with average Si core diameters, after annealing in dry oxygen up to 800 °C, of (a) 2.0 nm, (b) 3.5 nm, and (c) 4.7 nm.

It is noted that the visible components of the PL spectra from these passivated nc-Si were very broad, and that as the nanocrystal size was reduced, PL broadening accompanied PL blueshift. The width of the observed PL could be explained by the distributions of sizes in nc-Si, and therefore of energy gaps. For example, curve (a) in figure 3.21 has a PL with a FWHM of about 1 eV and a size dispersion of about 2 nm, FWHM. This observed PL width is about 0.2-0.6 eV narrower than calculated bandwidths for interband transitions in Si nanocrystals.[61,62]

It is of interest to compare the energies of the observed emission bands with recent calculations of photon energies of interband recombination transitions in Si nanocrystals. The calculations of PL energy versus nc-Si diameter from references 61 and 62 are shown in figure 3.22. In this figure, the dotted curve corresponds to the result from reference 61,which comes from solving the time dependent Schrodinger equation with a tight binding hamiltonian and a nonperturbative electron-hole Coulomb interaction. The solid curve corresponds to reference 62, which comes from a pseudopotential calculation. The solid circles represent PL peak energies measured from the samples of oxygen passivated nc-Si. The error bars represent size distributions. The shaded area represents the region of PL intensity measured from the hydrogen passivated nc-Si, for which no emission peaks were observed above 1.2 eV. As can be observed, there are differences in the measured PL peak energies from oxygen and hydrogen passivated nc-Si. The

PL peak energies from oxygen passivated nc-Si seem to fit reference 62 better, while the ones from hydrogen passivated nc-Si are below both calculated curves. From figure 3.22, it is also clear that increased PL broadening due to dispersion of nanocrystal size is expected as the average size of nc-Si decreases. This is because quantum confinement effects are stronger in smaller nanocrystals.

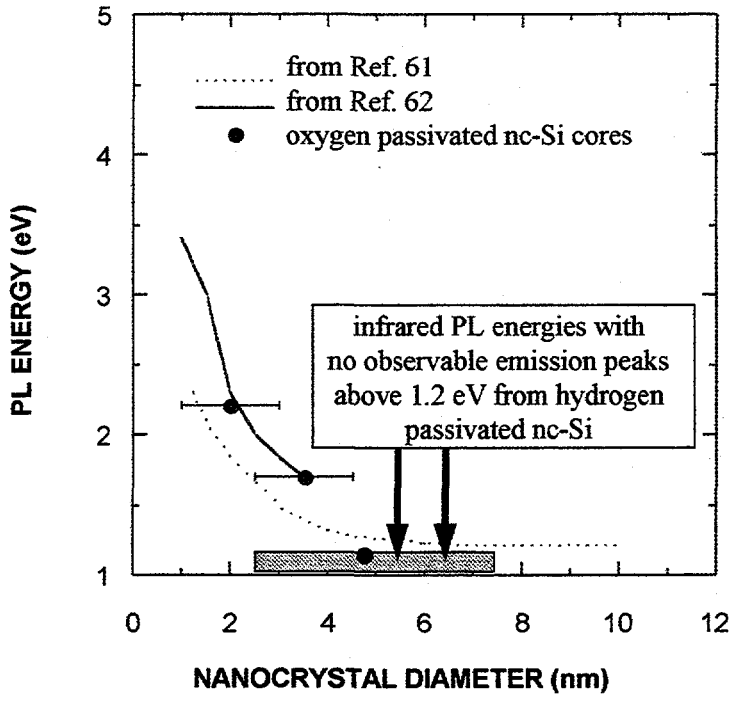

Figure 3.22 Theoretical PL energy vs nanocrystal diameter for nc-Si from reference [61] and reference [62]. Experimental values are from figure 3.20 and figure 3.21 of this work. Error bars represent size distributions.

The comparison between the experimental energies and the calculations suggests that the observed emissions could result from electron-hole recombination

transitions in the Si cores. However, the observed PL energies and PL broadening with reduction of nanocrystal size can also be explained by a model involving absorption in the quantum confined Si cores, and emission due to transitions between dangling bond or defect states in the passivation layers. This latter point will be discussed more in detail in the next section.

PL decay times for passivated nc-Si varied from sample to sample, but were observed to increase for lower emission energies, as reported for porous Si by some other workers.[63,64]

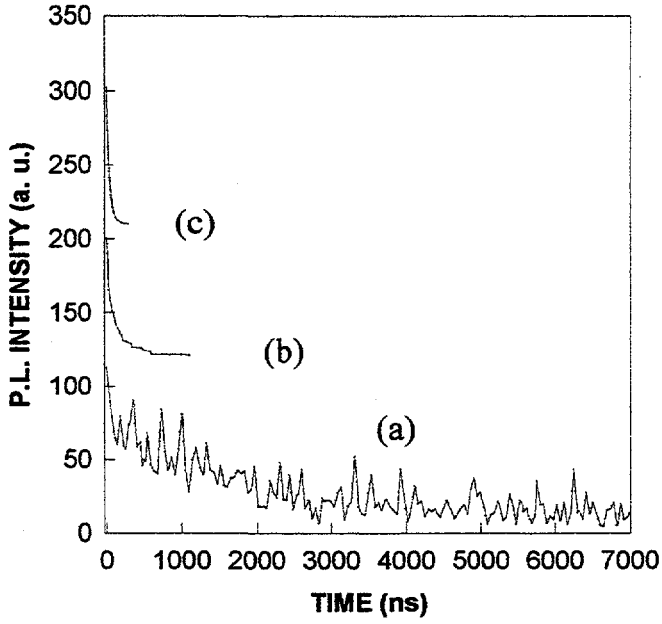

Figure 3.23 PL decay times from (a) oxygen passivated nc-Si with orange-white PL, (b) oxygen passivated nc-Si with bright red PL, and (c) hydrogen passivated nc-Si with infrared PL.

In figure 3.23, the top curve represents a PL decay time faster than the laser pulse (20 ns) from the oxygen passivated nc-Si sample with orange-white PL (bottom curve in figure 3.21). The middle curve represents a single exponential PL decay with a time constant of about 70 ns from the oxygen passivated nc-Si sample with bright red PL (middle curve in figure 3.21). The bottom curve represents a single exponential PL decay with a time constant of 2 μs from the hydrogen passivated nc-Si sample with infrared PL (topmost curve in figure 3.20).[65] Here, some similarities between PL decay times of these passivated nc-Si and porous Si are observed. Porous Si with red emission usually has PL decay times on the order of microseconds, while green or blue PL from oxidized porous Si usually has decay times on the order of nanoseconds or less.[9,64,66,67]

Figure 3.24 shows the PLE spectrum from a 50 nm thick sample of oxygen passivated nc-Si (curve (b)). This was the same sample that yielded the PL in curve (a) of figure 3.21. For a film much thinner than the attenuation length of the exciting light, PLE data are proportional to the absortion coefficient of the film as described in the chapter on experimental procedure. In fact, this PLE data curve qualitatively resembles the absorption coefficient (curve (a), offset by an arbitrary multiplicative factor) calculated from the Maxwell-Garnett formula[68] using the dielectric function of bulk Si.[69] This formula, which allows the calculation of the effective absorption coefficient of a composite medium consisting of Si dots embedded in an SiO_2 matrix, is written:[70]

$$\frac{\varepsilon_{eff}(\omega)-1}{\varepsilon_{eff}(\omega)+2} = \mathrm{p}\frac{\varepsilon\ (\omega)-1}{\varepsilon\ (\omega)+2} \tag{40}$$

Here p is the average volume fraction occupied by the Si dots. $\varepsilon(\omega)$ is the complex frequency dependent ratio of the dielectric function of bulk Si to the dielectric function of SiO_2. And $\varepsilon_{eff}(\omega)$ is the complex effective dielectric function of the composite medium. The frequency dependent absorption coefficient $\alpha(\omega)$ of the composite medium is given by

$$\alpha(\omega) \propto \omega\, \mathrm{Im}[\varepsilon_{eff}(\omega)] \tag{41}$$

where $\mathrm{Im}[\varepsilon_{eff}(\omega)]$ is the imaginary part of the complex effective dielectric function of the composite medium. This Maxwell-Garnett effective absorption coefficient curve was derived from Equations [40] and [41], for a system of Si dots with average diameter of 2 nm and a size distribution as in curve (b) of figure 1, embedded in a SiO_2 matrix.[71] Although the use of the bulk si value for $\varepsilon(\omega)$ does not account for the effects of band structure changes due to quantum confinement in the nc-Si, it is certainly suitable for a rough comparison with the PLE spectra. Note that since both curves in figure 3.24 have been normalized by arbitrary multiplicative factors, only the shapes of these curves can be compared, not their absolute values. In general, the PLE data and the calculated absorption coefficient have similar shapes. A steep rise in the absorption starting above 4.1 eV, and an absorption plateau between 3.5 eV and 4.1 eV are observed in both the PLE and

Maxwell-Garnett curves. However, in the energy range below the bulk direct interband transition of about 3.2 eV, the experimental PLE curve has a magnitude that is much greater than the calculated curve. This difference may be due to defect absorption in the SiO_x ($0 < x \leq 2$) layers covering the Si dots, which was, of course, not included in the Maxwell-Garnett calculation.

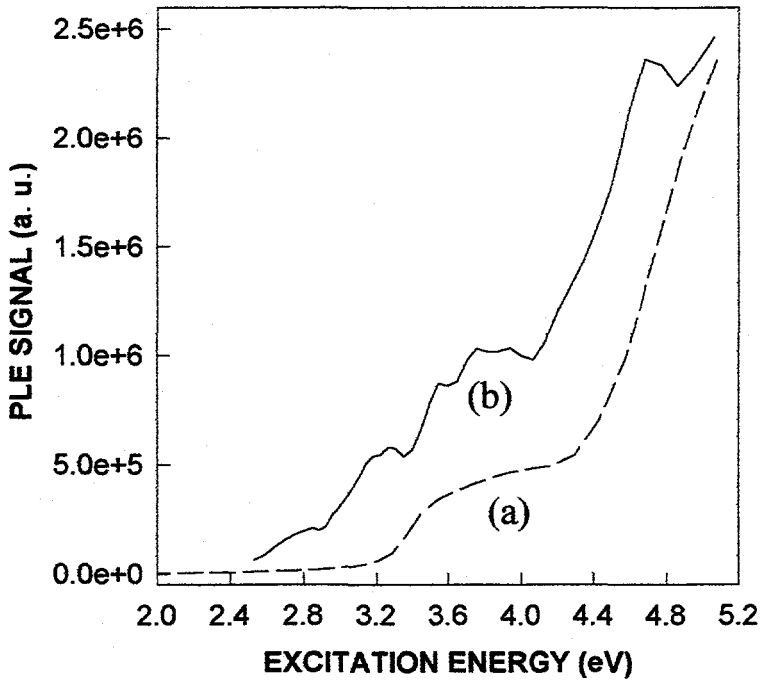

Figure 3.24 Normalized PLE spectrum of a sample of oxygen passivated nc-Si with average Si cores of 2 nm (curve b), and the normalized absorption coefficient derived from Maxwell-Garnett formula using bulk Si dielectric function for a system of Si dots of average diameters of 2 nm (curve a).

The experimental PLE curve also has structures that are not found on the calculated curve. These structures are real and reproducible. They could be due either to absorption from various defects in the SiO_x ($0 < x \leq 2$) layers covering the nc-Si or the quantization of electronic density of states of small dots, or both. It is most likely, however, that these structures result from defect absorption in SiO_x, since they are also seen in the energy range below 3.2 eV, where the absorption coefficient of bulk Si is very small. It is concluded from the above discussion that, apart from a small contribution from defect absorption, strong absorption in the quantum confined Si cores of the passivated nc-Si creates the excitations responsible for the PL.

For all samples of oxygen passivated nc-Si, the PL intensities increased after annealing in dry oxygen at 4×10^{-4} Torr up to 800 °C, without any accompanying PL peak shift. But a slight reduction in PL intensity was observed after post annealing to 900 °C. Figure 3.25 shows the effect of annealing at up to 800 °C in dry O_2 on PL intensity of the same sample as in curve (a) of figure 3.21. Similar behavior has also been observed for porous Si and Si ultra-fine particles.[50,72,73] The inset of figure 3.25 shows XPS data from the same sample as a function of annealing in oxygen. The peak near 99.5 eV binding energy is due to photoelectrons from the Si 2p core-level transition in bulk crystalline Si. This peak shifts to about 103.5 eV for SiO_2. Smaller shifts are expected for intermediate

oxidation states of Si in SiO_X ($0 < x < 2$). These data show that the ratios of SiO_X to Si ($0 < x \leq 2$) increase as a function of annealing temperature from 500 °C to 800 °C. Note that the absence of a peak near 99.5 eV in the upper XPS curve in the inset does not imply that the nc-Si crystallites have been completely oxidized, because XPS is a surface sensitive technique and a signal from a silicon core may be unobservable[47,74]. Moreover, HRTEM and PLE measurements on the same sample have shown the existence of unoxidized Si cores after oxidation (curve 1(b), figure 3.17, and figure 3.24).

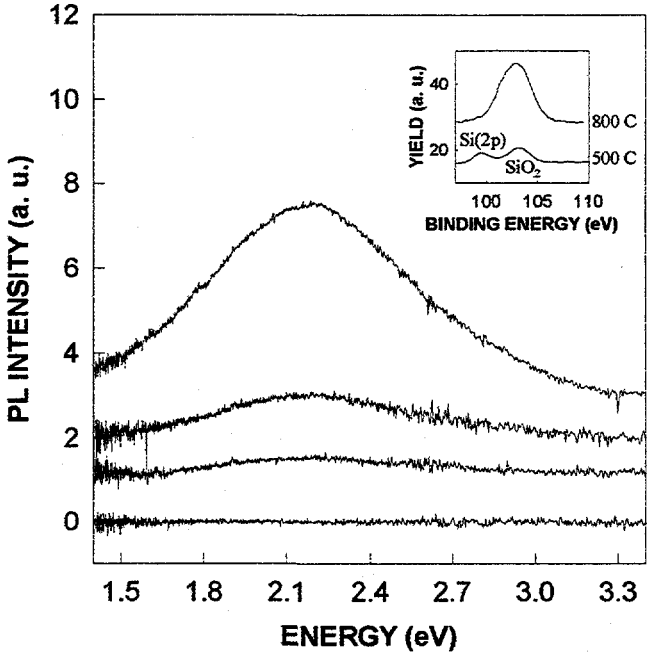

Figure 3-25 PL intensities of a sample of oxygen passivated nc-Si as a function of annealing temperatures from 25 °C to 800 °C. The inset shows XPS signals from the same sample.

My speculation is that the thickness of the Si oxide outer layer has been established by the low temperature annealing. Nevertheless, this SiO_x layer had a significant amount of Si and oxygen dangling bonds, thus a nonstoichiometric Si/O ratio. Short annealing at higher temperatures simply passivated the dangling bonds more effectively, therefore achieving a more stoichiometric Si/O ratio (with x increased toward 2), leading to improved PL intensity without any accompanying PL peak shift. Nonetheless, a reduction in PL intensity at an annealing temperature of about 900 °C is not a complete surprise. The native sub-oxide layer grown on a Si wafer by air exposure is known to begin to vaporize at temperatures ≥ 850 °C[75]; so when the rate of Si sub-oxide vaporization is comparable to the corresponding rate of formation, dangling bonds could be produced at the Si-SiO_x interface of the nc-Si, and a reduction in PL intensity would be not be unexpected.

3.4b Amorphous Si oxide nanostructures (an-SiO_x)

Figure 3.26 shows a typical AES spectrum for a sample of an-SiO_x synthesized by vaporization of Si in an O_2 buffer gas. The composition of the an-SiO_x was mostly SiO_x ($0<x\leq2$), since there was almost no signal from the elemental Si (LMM) Auger transition in the AES spectrum at 92 eV. The O (KLL) Auger transition was observed at 503 eV. Note that no contamination was observed from the carbon

boat or the tungsten basket. HRTEM revealed that these an-SiO_x films were networks of interlinking amorphous Si oxide nanostructures with occasional embedded Si dots. Figure 3.27 shows a TEM image of a typical sample of an-SiO_x.

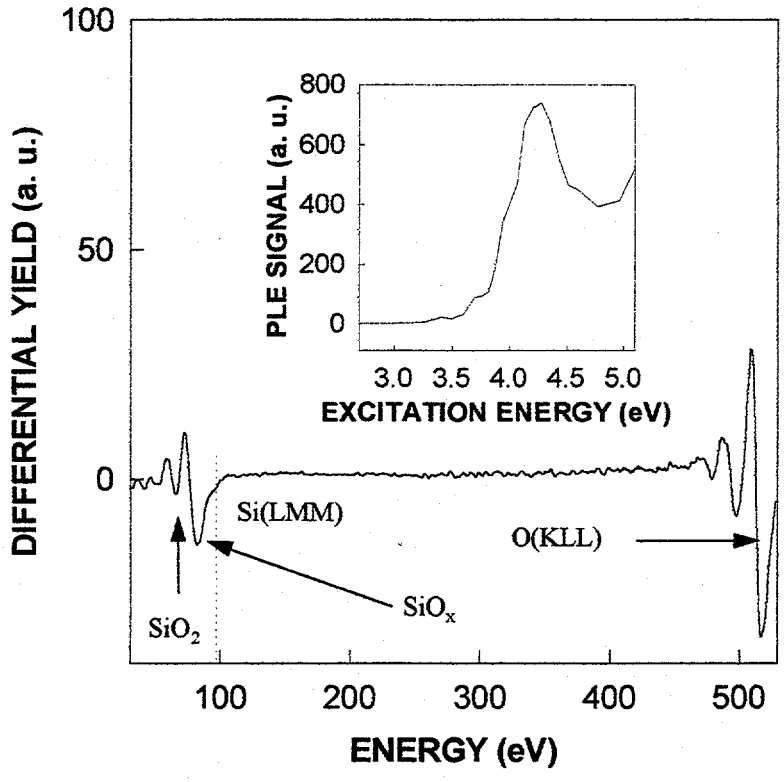

Figure 3.26 Typical AES spectrum for an-SiO_x synthesized by vaporization of Si in an O_2 buffer gas. The inset shows the normalized PLE spectrum of the same sample.

The inset of figure 3.26 shows a PLE spectrum of the same sample that yielded the AES curve in figure 3.26. This sample of an-SiO_x was deposited on HOPG by

vaporization of Si at 1600 °C, in an O_2 buffer gas of 3.5 mTorr, and at a source to substrate distance of 8 cm. This PLE spectrum curve does not resemble that due to Si absorption (compare with figure 3.24). Therefore, the contribution of the occasionally embedded small Si dots to the net absorption is negligible. The excitation spectrum of an-SiO_x in figure 3.26 is similar to absorption spectra observed in non-stoichiometric SiO_x. For example, a strong absorption peak at about 4.2-4.3 eV was observed and identified with a type of oxygen deficiency defect center in silica.[49,76,77] The strong absorption in the energy range > 5 eV in the PLE spectrum in figure 3.26 has also been reported for certain types of oxygen related defect centers in silica.[49,76]

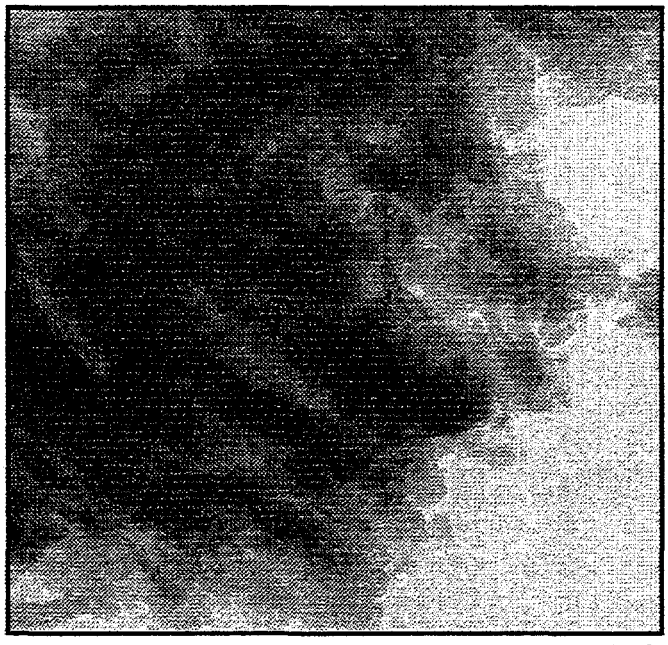

Figure 3.27 TEM image of a sample of an-SiO_x

Figure 3.28 shows PL spectra for two samples of an-SiO_x. Curve (a) was from the same sample that yielded the PLE spectrum in figure 3.26. This sample exhibited a strong and very broad orange-white PL, peaked at about 2.2 eV, with a bi-exponential PL decay with time constants of 1.2 μs and 7.8 μs (inset of figure 3.28). Note that the emission energies in this sample were much smaller than the absorption threshold energy. This indicates the existence of optical emission between trap states or lower energy defect levels, which have absorption efficiencies several orders of magnitude smaller than the 4.3 eV absorption band.[49,77,78] The emission process is usually sensitive to such trapping states.[78] Also, broad PL peaks at about 1.9 eV and 2.3 eV were observed for oxygen related defect centers in amorphous Si oxide.[77] The PL decay of these centers was non-exponential with decay times from hundreds of nanoseconds to many tens of microseconds. The observed broad PL in curve (a) may originate from a combination of these two defect centers. Curve (b) was from a sample of an-SiO_x deposited on a Si wafer, which had been covered with a native oxide layer due to long exposure to ambient atmosphere. This sample was prepared by vaporization of Si at 1600 °C, in an O_2 buffer gas pressure of 2 mTorr, and at a source to substrate distance of 7 cm. There are several PL peaks recorded at around 1.7-1.9 eV, 2.2-2.5 eV, and 2.6-3.1 eV. All these PL bands have been reported for different types of oxygen related defects in Si oxide.[5,77,79] I conclude that the emission and absorption from an-SiO_x are dominated by defect centers in the oxide.

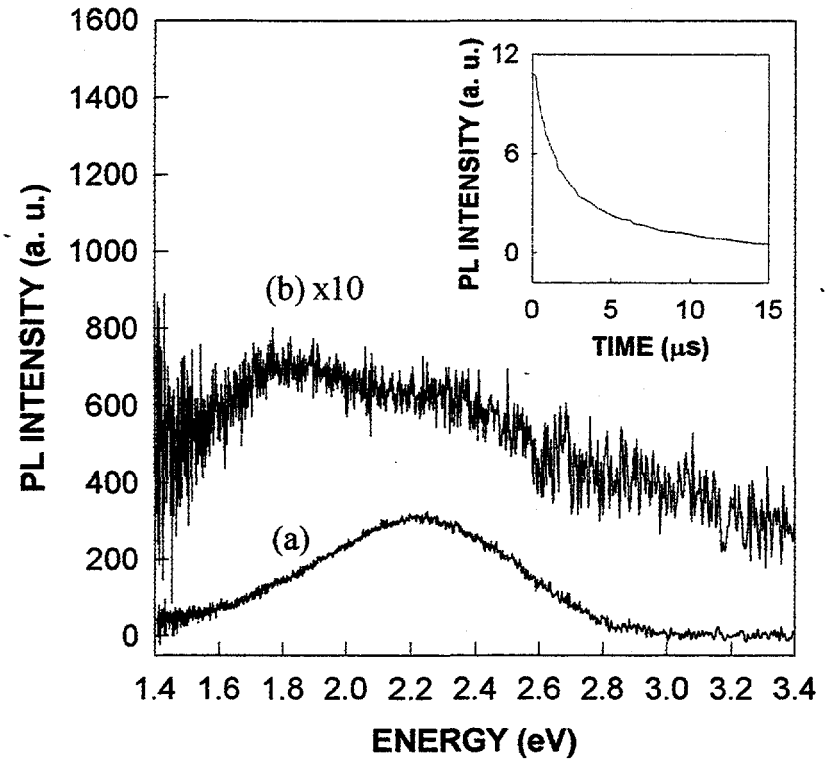

Figure 3.28 PL spectra of an-SiO_x synthesized by vaporization of Si (a) at 1600 °C in an O_2 buffer gas of 3.5 mTorr and a source to substrate distance of 8 cm, and (b) by vaporization of Si at 1600 °C in an O_2 buffer gas of 2 mTorr and a source to substrate distance of 7 cm. The inset shows PL decay time of sample (a).

Similar to the case of oxygen passivated nc-Si, the PL intensities of these two an-SiO_x samples increased with annealing in dry oxygen at 4×10^{-4} Torr up to 800 ° C without any PL peak shift. So, even though all an-SiO_x samples were composed mostly of SiO_x ($0<x\leq2$), they shared many common PL properties with oxygen

passivated nc-Si: very broad PL, many PL peaks in similar energy regions, and increasing PL intensities without PL peak shift after annealing in dry oxygen.

3.4c Discussion

The experiments presented in this thesis show that, for passivated nc-Si, absorption occurs between the quantum confined electronic states of the Si cores. PL blue shifts occur as the size of nc-Si crystallites is reduced. These observations clearly indicate the importance of the quantum confinement effects on the optical absorption properties of nc-Si. This latter point has received direct supports from recent x-ray absorption spectroscopy (XAS) experiments.[80] Figure 3.29 shows the XAS spectra of the L-edge absorption of bulk Si (a), nc-Si with average size of 2.8 nm (b), and nc-Si with average size of 1.0 nm (c). The L-edge absorption measures the energy separation between the 2p core level and the bottom of the conduction band. Consequently, quantum confinement effects, which raise the energy of the bottom of the conduction band, increase the absorption threshold by the same amount. The quantum confinement effects induced upshift of the bottom of the conduction band are found to be about 0.5 eV and 0.3 eV for nc-Si with average size of 1.0 nm and 2.8 nm (as measured by an AFM[81]) respectively. Due to the selection rule for electric dipole transition (change in angular momentum: $\Delta\, l = \pm 1$), the L-edge probes the s and d density of states of the conduction band. The doublet features at about 99.8 eV, 100.7 eV and 102.5 eV in the XAS spectrum of bulk Si in curve (a) are due to the spin orbit splitting of the Si $2p_{3/2}$ and Si $2p_{1/2}$ levels, which are separated by 0.61 eV[82] and are convoluted with the s and d density of states of the conduction band. These doublet features are significantly washed out or unobservable in the L-

edge XAS spectra of nc-Si, because these nc-Si have a spread in sizes. Similar results have been reported for the L-edge absorption spectra of porous Si which contains Si nanocrystals with a spread in sizes.[83] The total increase in the band gaps of nc-Si are expected to be greater than the measured increase in the L-edge absorption, since it includes the downshift of the top of the valence band as well.

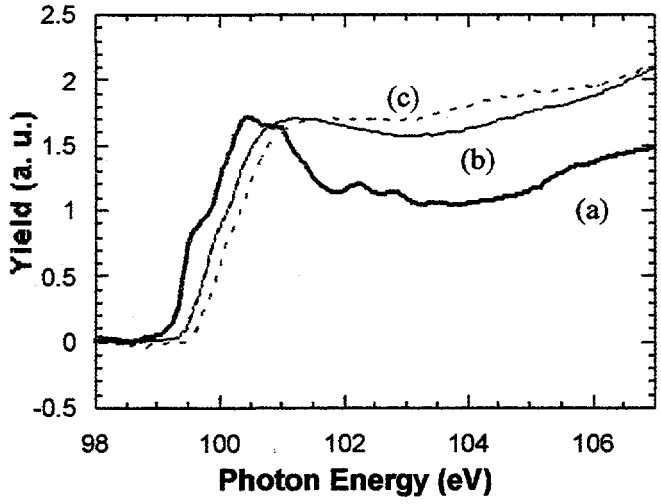

Figure 3.29 L-edge absorption of bulk Si (a), nc-Si with average size of 2.8 nm (b), and 1.0 nm (c).

As far as the PL mechanism is concerned, it seems that a simple band to band recombination mechanism within the Si cores cannot be ruled out. There are, however, some properties of the PL that suggest a different explanation: 1) the differences in PL spectra of hydrogen passivated nc-Si and of oxygen passivated nc-Si; 2) the PL properties of the oxygen passivated nc-Si have some similarities to those of the an-SiO_x samples, for which oxide defect states apparently play a

dominant role in the PL; and 3) the theory of quantum confinement effects cannot account for the short and exponential PL decay times (nanoseconds) of oxygen passivated nc-Si.[67] These properties lead to the belief that defect centers, rather than band-to-band recombination in the Si nanocrystals, are more likely to be responsible for the PL of the nc-Si films.

For many nanocrystals of comparable sizes, hydrogen passivated nc-Si had PL spectra that were redshifted in comparison with the corresponding PL spectra from oxygen passivated nc-Si (curves 3.20(a) and 3.21(b)). In addition, the PL intensities from hydrogen passivated nc-Si films were usually weaker than those from oxygen passivated nc-Si films of comparable thicknesses. These effects may have been caused by imperfect passivation of the hydrogen passivated nc-Si in this work, and they indicate a strong influence of surface and/or interface states in the recombination process of nc-Si. [7,9,10,14,63,64] . The facts that PL decay times of the passivated nc-Si in this work varied widely from sample to sample, and that oxygen passivated nc-Si had PL decay times much shorter than accounted for by the quantum confinement effects imply the coexistence of competing radiative and non-radiative recombination processes. These competing processes may be related to surface conditions such as residual dangling bonds, surface stress and/or strain, and Si oxide defects at/or near the surface[9,10,63]. In fact, the many common PL properties for oxygen passivated nc-Si and an-SiO_x, pointed out at the end of section 3.4b, suggest that the radiative recombination processes in both materials

are dominated by transition through defect centers. These defect centers are located in the oxide layer or at the boundary between this layer and the Si crystallite.[5,9,79] A conclusion will be reached by discussing these properties with reference to this alternative model of the PL in nc-Si.

It is noticed that the data concerning passivated nc-Si can be best explained by a model involving absorption in the quantum confined Si cores and emission which involves electronic transitions between surface and/or interface states.[7, 9,10,79] This model can explain PL blueshifts with decreasing nanocrystal size, as well as the surface sensitive property of the PL from nc-Si. This model can also explain qualitatively the PL blue shift with decreasing nanocrystal size, accompanied by PL broadening, observed in the presented PL data. Figure 3.30 is a diagram showing the energy levels near the surface of two sizes of Si quantum dots.

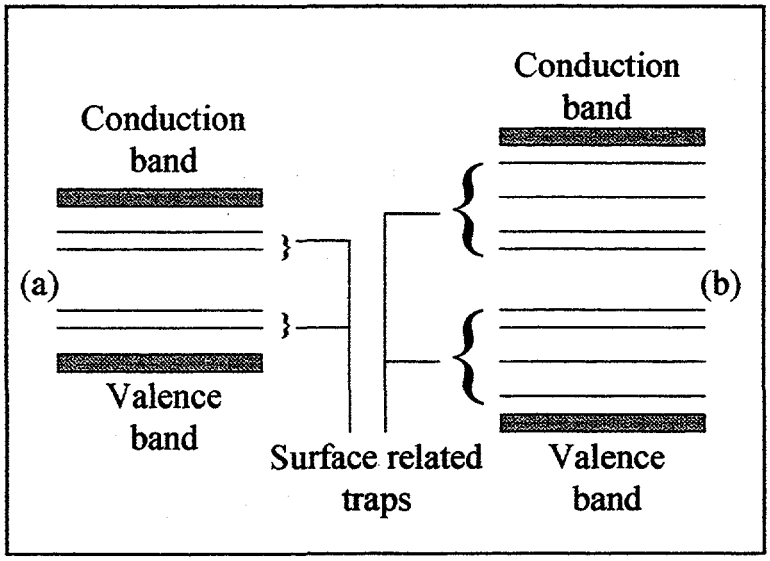

Figure 3.30 Energy diagrams, including surface related traps, of (a) large quantum dots, and (b) small quantum dots.

It should be noted that these diagrams refer to ensembles of dots of a given size; the detailed energy levels for a particular size may vary from dot to dot depending on surface/interface configuration. In (a), the dots are bigger than the ones in (b) which have larger quantum confined energy gaps. Upon absorption of photons of proper energies, electrons and holes are generated in the conduction and valence bands of the dots. But due to the existence of surface related traps with energy levels extending into the energy gaps, there is a possibility of carriers getting trapped by, and subsequently recombined through, these gap states. A PL blueshift with reducing nanocrystal size is possible, since carriers generated in the smaller dots may have access to gap states with trapping energies higher than the energy gap of the bigger dots. Broad PL spectra are also expected. On the basis of the diagram in figure 3.30, it might be expected, indeed, that the PL bandwidth will increase with increasing energy gap. This is because carriers generated in the smaller dots may also have access to gap states with much smaller trapping energies. So, depending on the relative densities and recombination efficiencies of the different surface states involved, a PL broadening may accompany the PL blue shift of the smaller dots. This has been observed in the data in figure 3.21, where the bandwidth in curve (a) is substantially larger than the visible counterpart in (b). The different properties of oxygen and hydrogen passivated dots reflect the differences in the energy distribution, lifetimes, and other properties of the surface or interface states. In particular, the longer wavelength emission in hydrogen

passivated dots is caused by a prevalence of surface states lying deeper in the energy gap than for oxygen passivated dots.

In conclusion, nc-Si with controllable size have been synthesized by the technique of gas aggregation. When passivated by hydrogen or oxygen, these nc-Si showed strong infrared and/or visible PL. The PL properties of these nc-Si can be best explained by a model involving absorption in the quantum confined Si cores and emission due to transition between defect states in the passivation layer.

4. Conclusion

In conclusion, Si nanoclusters have been synthesized, with well controlled surface chemistry, by laser ablation of Si followed by substrate annealing, laser ablation of Si in an Ar buffer gas, and thermal vaporization of Si in an Ar buffer gas. Si oxide nanostructures were also synthesized by using O_2 as the buffer gas instead of Ar during the deposition.

The technique of laser ablation of Si followed by substrate annealing is capable of producing only less than a layer of Si nanoclusters on a graphite substrate. Surface passivation of these clusters with atomic hydrogen or oxygen did not result in any detectable visible PL, probably due to nonradiative decay of excition in the Si cores to the graphite subtrate. But prolonged ambient air

exposure of these clusters produced strong and stable red to green-blue PL, which can be attributed to the completely oxidized clusters.

The technique of laser ablation of Si in an Ar buffer gas is capable of producing multilayer films of Si nanoclusters. However, the size distribution of the clusters obtained from this technique is very wide, ranging from a few nanometers to many micrometers. This wide size distribution makes it difficult to study the effect of size on the electronic and/or optical properties of the generated clusters.

The technique of thermal vaporization of Si in an Ar buffer gas is capable of producing multilayer films of Si nanoclusters with fairly narrow size distributions. The average cluster size in this technique can be controlled with parameters such as Si source temperature, Ar buffer gas pressure, and source to substrate distance. HRTEM and XRD revealed that these nanoclusters were crystalline in nature. However, during synthesis, if oxygen was the buffer gas, a network of amorphous Si oxide was formed.

The electronic and optical properties of these nc-Si were studied by XAS, PL, PLE, PL decay, and scanning tunneling spectroscopies.

Although capable of producing reliably ELDS for clean and atomically smooth substrate surfaces, STS fails to reveal the ELDS of Si clusters which sit loosely on substrate surface by just Van der Waals and/or electrostatic forces (due to the lack of a good electrical contact).

When passivated with atomic hydrogen or oxygen, these nc-Si showed strong infrared and/or visible PL with PL decay time increasing with longer emission wavelength. Absorption in the Si cores for surface passivated nc-Si, but mainly in oxygen related defect centers for an-SiO_x, was observed by PLE spectroscopy. As the average size of nc-Si was reduced, the bottom of the conduction band of these nc-Si was observed to upshift. The visible components of PL spectra were also noted to blue shift and broaden as the size of the nc-Si was reduced. There were differences in PL spectra for hydrogen and oxygen passivated nc-Si, but many common PL properties between oxygen passivated nc-Si and an-SiO_x were noted. The data in this work can be best explained by a model involving absorption between quantum confined states in the Si cores and emission between surface and/or interface states.

So, the results of this work point to the importance of the quantum confinement effects in the electronic structures and optical absorption properties of nc-Si, as well as the consequence of the presence of surface/interface states in the overall electronic and optical recombination properties of nc-Si. In other words, unless a defect free surface passivation layer is achieved, the ultimate properties of these Si quantum dots will be jointly determined by both the quantum confinement effects and surface/interface states.

Appendix I

Radiative defect centers in silicon oxide

Many different defect centers may exist in silicon oxide. These can be related to an oxygen ion vacancy, a Si ion vacancy, a broken bond, or some imperfection in the silicon oxide lattice structure. Analogous to the case of an electron in a hydrogen atom, carriers that are trapped at these localized defect centers, may be promoted to some excited states of the trap centers, and in some cases may radiatively relax to the ground states of the corresponding traps.

Radiative centers may also exist at the Si-SiO_2 interface. A type of such defects is known to have a sharp excitation onset at around 4.3 eV and a PL peak at around 2.3-2.7 eV. The energy of 4.3 eV is known as the difference between the Si valence states and SiO_2 conduction band at the macroscopic Si-SiO_2 interface.[78,85] In experiments performed on SIMOX (Si isolation by implantation of oxygen) structures photoinduced charge trapping is observed.[86] It is suggested that the onset observed at photon energy of 4.3 eV corresponds to ejection of an electron from Si into the oxide. This electron may relax nonradiatively to some lower energy interface state before a final radiative recombination with the hole, causing the PL peak energy to be smaller than the excitation energy.

Another well-studied type of defect center is known as nonbridging oxygen hole center (NBOHC). These centers have been reported in silica optical fibers and they

luminesce in the red (1.65-1.9 eV) at room temperature, with a peak width (FWHM) of around 0.35 eV.[87-90] Actually, three different types of NBOHC have been identified which vary in PL energies and quantum efficiencies.[5,16] The first type of NBOHC is Si-O^-, which exhibit a weak red PL which does not shift appreciably with heat treatment. The second type of NBOHC is stabilized with a hydrogen bond, such as Si-O^--.....-H-Si. This type of defect is seen in silica containing high concentration of hydroxyls or hydrides, and exists only at temperatures below 350 °C. Its PL has been shown to blueshift and increase in quantum efficiency with increasing hydrogen content. The third type of NBOHC is related to the strain of bonding at an interface between two materials of different bond lengths, density, or structure. This type of NBOHC has been reported after the drawing of oxide clad fibers and after high temperature annealing. Finally, the type of NBOHC which are stable at high temperatures (as high as 800 °C) do not show any PL line shift or shape change during heating to high temperatures compared to PL at room temperature. Clusters of NBOHC have also been reported to have absorption peaks in the 2 and 4.75 eV range, and PL peak at around 1.7 eV. Following is a drawing of isolated NBOHC and NBOHC clusters near the Si-SiO_2 interface and deep in the silicon oxide layer taken from reference [5].

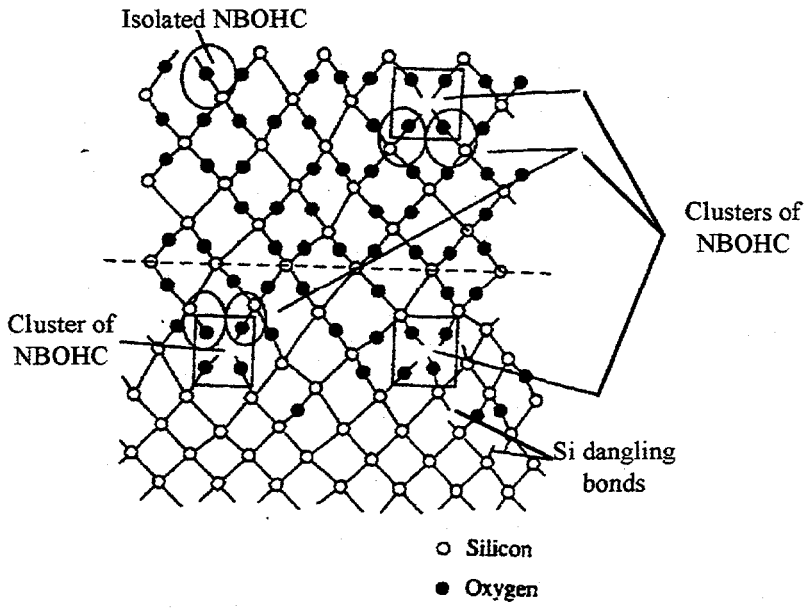

Another defect in amorphous SiO_2 known as two fold coordinated silicon has an absorption band at 5.03 eV and two luminescence bands at 4.3 eV and 2.65 eV.[76] The model assigned to this center is a silicon atom with only two neighboring oxygens.

Oxygen-deficient silica has been observed to have a strong PL band at around 2.7 eV, while high-OH silica are known to produce PL bands at 3.1 eV and 4.2 eV under 7.9 eV excitation.[49] Various other forms of oxygen deficiency in the SiO_2 network or nanoclusters are also known to produce PL peaks at 1.9, 2.2, 2.7, 3.1, and 4.3eV.[77,79]

Appendix II

(Adapted according to reference [91])

A method for the deconvolution of experimental PL decay curves

An experimental PL decay curve usually has the form:

$$F(x) = \int_{-\infty}^{+\infty} f(u)S(x-u)du \qquad \text{(a1)}$$

where $F(x)$ is the observed PL decay spectrum, $f(x)$ is the true PL decay profile, and $S(x)$ is the slit function or intrinsic broadening function (a combination of all the resolution effects, including the profile of the exciting laser pulse). $S(x)$ can be determined experimentally by taking a decay curve of the laser pulse itself.

Fourier transform both sides of equation [a1] to get:

$$\bar{F}(t) = \bar{f}(t)\bar{S}(t) \qquad \text{(a2)}$$

where the bar represents Fourier transform.

Dividing by $\bar{S}(t)$ and taking the inverse transform:

$$f(x) = \int_{-\infty}^{+\infty} \bar{F}(t)T(t)\exp(2\pi\ itx)dt \qquad \text{(a3)}$$

where T(t) denotes the reciprocal of $\bar{S}(t)$

Substitute $\bar{F}(t) = \int_{-\infty}^{+\infty} F(x)\exp(-2\pi\ itx)dx$ into equation [a3]:

$$f(x) = \int_{-\infty}^{+\infty} F(u)du \int_{-\infty}^{+\infty} T(t)\exp\{(2\pi\ it(x-u)\}dt \qquad \text{(a4)}$$

Let the second integral on the right hand side of equation (a4) be denoted by $J(x-u)$ then

$$J(x-u) = \int_{-\infty}^{+\infty} T(t)\exp\{(2\pi\ it(x-u)\}dt \qquad \text{(a5)}$$

Assume an exponential slit function such that $S(x) = \frac{1}{2}\alpha\ \exp(-\alpha|x|)$ (a6)

where $S(x)$ has been normalized so that $\int_{-\infty}^{+\infty} S(x)dx = 1$ and α is a constant. Then

$$\overline{S}(t) = \frac{\alpha^2}{\alpha^2 + 4\pi^2 t^2} \qquad \text{(a7)}$$

and $J(x-u) = \int_{-\infty}^{+\infty} (1 + \frac{4\pi^2 t^2}{\alpha^2})\exp\{2\pi\ it(x-u)\}dt$

$$= \delta(x - u) - \frac{1}{\alpha^2}\delta^{II}(x - u) \qquad \text{(a8)}$$

where $\delta(x - u)$ is the Dirac delta function defined as:

$$\delta(x - u) = \lim_{\varepsilon \to 0} \int_{-\infty}^{+\infty} \exp(-\varepsilon\ t^2)\exp\{2\pi\ it(x-u)\}dt \qquad \text{(a9)}$$

and $\delta^{II}(x - u)$ represents the second derivative of $\delta(x - u)$.

Plug the value of $J(x-u)$ in equation [a8] into equation [a4] to see:

$$f(x) = F(x) - \frac{1}{\alpha^2}F^{II}(x) \qquad \text{(a10)}$$

Equation [a10] relates the experimentally observed PL decay curve $F(x)$ and its second derivative with the true profile of the PL decay.

However, if the slit function $S(x)$ is much shorter than the true PL decay curve $f(x)$, $S(x-u)$ in equation [a1] may be replaced by $\delta(x - u)$. In this case, equation [a1] becomes:

$$F(x) \approx f(x) \qquad \text{(a11)}$$

The PL decay time is then obtained by numerically fitting $f(x)$ with exponential decay expression of the form:

$A_1 \exp(-\beta_1)$ for monoexponential decay

or

$A_1 \exp(-\beta_1) + A_2 \exp(-\beta_2) + A_3 \exp(-\beta_3) + ...$ for multiexponential decay

where A_n and β_n represent the maximum PL intensity (PL intensity at time $t = 0$) and the PL decay time.

Appendix III

(From reference 69 and reference 92)

Table of index of refraction and extinction coefficient for Si and Si oxide

λ(nm)	n (SiO2)	k (SiO2)	n (Si)	k (Si)
244.3	1.511257	0	1.683	3.508
253.16	1.506817	0	1.722	3.774
262.03	1.50282	0	1.839	4.183
270.89	1.499208	0	2.19	4.76
279.75	1.495934	0	3.026	5.243
288.61	1.492957	0	4.231	5.261
297.47	1.490243	0	5.009	4.358
306.33	1.48776	0	5.077	3.718
315.19	1.485484	0	5.083	3.385
324.05	1.483392	0	5.12	3.188
332.91	1.481464	0	5.206	3.038
341.77	1.479685	0	5.323	2.937
350.63	1.478039	0	5.506	2.905
359.49	1.476513	0	5.977	2.916
368.35	1.475096	0	6.79	2.272
377.22	1.473778	0	6.721	1.112
386.08	1.472549	0	6.169	0.568
394.94	1.471402	0	5.767	0.365
403.8	1.47033	0	5.467	0.26
412.66	1.469326	0	5.239	0.199
421.52	1.468385	0	5.06	0.16
430.38	1.467501	0	4.916	0.132
439.24	1.46667	0	4.8	0.111
448.1	1.465888	0	4.694	0.096
456.96	1.465151	0	4.603	0.083
465.82	1.464456	0	4.522	0.073
474.68	1.463799	0	4.452	0.064
483.54	1.463178	0	4.389	0.058
492.41	1.462591	0	4.332	0.052
501.27	1.462034	0	4.283	0.046
510.13	1.461506	0	4.236	0.042
518.99	1.461004	0	4.195	0.038
527.85	1.460528	0	4.157	0.035
536.71	1.460075	0	4.122	0.033
545.57	1.459644	0	4.092	0.03
554.43	1.459234	0	4.059	0.028
563.29	1.458843	0	4.032	0.025
572.15	1.45847	0	4.007	0.024
581.01	1.458113	0	3.981	0.023
589.87	1.457773	0	3.96	0.022
607.59	1.457136	0	3.92	0.019
616.46	1.456839	0	3.9	0.018
625.32	1.456553	0	3.885	0.017
634.18	1.45628	0	3.87	0.016
643.04	1.456018	0	3.854	0.015

λ(nm)	n (SiO2)	k (SiO2)	n (Si)	k (Si)
651.9	1.455766	0	3.839	0.014
660.76	1.455525	0	3.827	0.014
669.62	1.455293	0	3.813	0.013
678.48	1.45507	0	3.8	0.0125
687.34	1.454855	0	3.788	0.012
696.2	1.545649	0	3.773	0.011
705.06	1.45445	0	3.766	0.011
713.92	1.454259	0	3.757	0.0092
722.78	1.454075	0	3.747	0.01
731.65	1.453897	0	3.737	0.01
740.51	1.453726	0	3.73	0.009
749.37	1.453561	0	3.721	0.007
758.23	1.453402	0	3.714	0.008
767.09	1.453248	0	3.706	0.0066
775.95	1.453099	0	3.698	0.0068
784.81	1.452955	0	3.691	0.005
793.67	1.452816	0	3.684	0.0085
802.53	1.452682	0	3.679	0.0065
811.39	1.452552	0	3.672	0.007
820.25	1.452426	0	3.666	0.005
829.11	1.452305	0	3.663	0.0058
837.97	1.452187	0	3.658	0.0044

Appendix IV

(Adapted according to reference [68])

Maxwell-Garnett formula for the absorption of light of a composite medium consisting of spherical semiconductor dots embedded in a dielectric host matrix

Consider first a single dielectric sphere of radius R and dielectric constant ε_1 embedded in an infinite medium with dielectric constant ε_2.

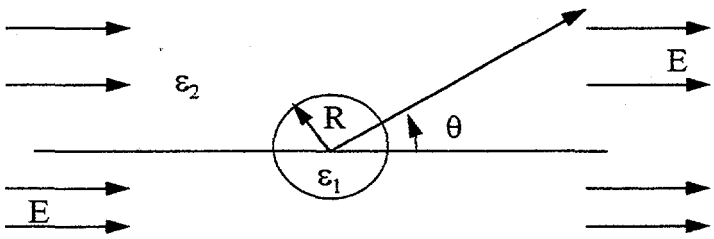

The potential V(r)- for a homogeneous, static field $\vec{E}$ oriented along the z-axis- inside and outside the sphere must satisfy the Laplace equation:

$$\nabla^2 V(r) = 0 \qquad \text{(A1)}$$

For infinite distance from the dot the potential has to behave like that of the homogeneous field,

$$V(r) \propto -\vec{E}.\vec{r} \qquad \text{(A2)}$$

At the boundary of the sphere the continuity of the tangential components of the field $\vec{E}$, respectively of the normal components of the induction field $\vec{D}$ must be assured.

$$V|_{r=R-0} = V|_{r=R+0} \tag{A3}$$

$$\varepsilon_1 \frac{\partial V}{\partial r}\bigg|_{r=R-0} = \varepsilon_2 \frac{\partial V}{\partial r}\bigg|_{r=R+0} \tag{A4}$$

Choosing solution of the form:

$$V_{inside} = \sum_{l=0}^{\infty} A_l r^l P_l(\cos\theta) \tag{A5}$$

and

$$V_{outside} = \sum_{l=0}^{\infty} [B_l r^l + C_l r^{-(l+1)}] P_l(\cos\theta) \tag{A6}$$

where $P_l(\cos\theta)$ is Legendre polynomials of order l, and A_l, B_l, C_l are normalization constants determined by the boundary conditions [A3] and [A4].

Using the potential forms given by [A5] and [A6] in the boundary condition equations [A3] and [A4] yields:

$$V_{inside} = -(\frac{3}{\varepsilon+2}) E\, r\cos\theta \tag{A7}$$

$$V_{outside} = -E\, r\cos\theta + \varepsilon_2 \frac{\varepsilon\ -1}{\varepsilon\ +2} R^3 \frac{E}{r^2}\cos\theta = -E\, r\cos\theta + \frac{d}{r^2}\cos\theta \tag{A8}$$

where $\varepsilon \equiv \frac{\varepsilon_1}{\varepsilon_2}$ and $d \equiv \varepsilon_2 \frac{\varepsilon\ -1}{\varepsilon\ +2} R^3 E$

So the potential inside the spherical dot is $\frac{3}{\varepsilon+2}$ times the potential outside, and the potential outside is a superposition of a homogeneous applied field and a dipole d placed at the center of the spherical dot.

Equation [A8] shows that for its surrounding medium, the dielectric sphere acts as a point dipole with the polarizability $\kappa = \frac{\varepsilon - 1}{\varepsilon + 2}\varepsilon_2 R^3$.

The above static (non propagating) electric field treatment has been shown [Sommerfeld (1949), Bottcher (1973)][93,94] to be valid for the case of propagating waves, provided $R << \lambda$. The only modification is that the static dielectric constants are replaced by the respective complex dielectric functions.

Now, consider the problem of several identical quantum dots homogeneously distributed inside the host material. The volume fraction of the quantum dot material is p.

If the dot radii are fairly smaller than the separation between the dots, it is possible to consider this system as a system of point-like dipoles.

The field E_1 acting on such a dipole has been computed by Sommerfeld[93] [Sommerfeld (1949)] as:

$$\vec{E}_1 = \vec{E} + \frac{4\pi}{3\varepsilon_2}\vec{P} \qquad \text{(A9)}$$

where $\vec{E}$ is the macroscopic field, and $\frac{4\pi}{3\varepsilon_2}\vec{P}$ is the field resulting from the local deviation of matter distribution from the average homogeneous situation. The macroscopic polarization $\vec{P}$ may be written as:

$$\vec{P} = n\vec{d} = n\kappa\ \vec{E}_1 \tag{A10}$$

where n is the concentration of the dipoles and $p = \frac{4\pi\ R^3}{3} n$.

Inserting [A10] into [A9] to find:

$$\vec{P} = \frac{(\varepsilon_{eff} - 1)\varepsilon_2}{4\pi}\vec{E} \tag{A11}$$

$$\text{with } \varepsilon_{eff} \equiv \frac{1 + \frac{8\pi}{3\varepsilon_2} n\kappa}{1 - \frac{4\pi}{3\varepsilon_2} n\kappa} = 1 + \frac{3p(\varepsilon - 1)}{(1-p)\varepsilon + 2 + p} \tag{A12}$$

Therefore, ε_{eff} is the effective macroscopic dielectric function of the dipole plus dielectric cladding system relative to the dielectric function ε_2 of the cladding. Taking into account the wavelength dependency of the propagating waves, equation [A12] can be written in the form:

$$\frac{\varepsilon_{eff}(\lambda\ ) - 1}{\varepsilon_{eff}(\lambda\ ) + 2} = p\frac{\varepsilon\ (\lambda\ ) - 1}{\varepsilon\ (\lambda\ ) + 2} \tag{A13}$$

Equation [A13] is known as the Maxwell-Garnett formula for composite media.

Appendix V

Obtaining the absorption coefficient (off by an arbitrary multiplicative factor) for a composite medium consisting of Si dots embedded in an SiO_2 matrix from the Maxwell-Garnett formula.

The Maxwell-Garnett formula is:

$$\frac{\varepsilon_{eff}-1}{\varepsilon_{eff}+2}=p\frac{\varepsilon-1}{\varepsilon+2}$$

This complex formula can be rewritten in term of two real equations as:

$$(1-p)[\varepsilon_1\varepsilon_{1eff}-\varepsilon_2\varepsilon_{2eff}]-(1+2p)\varepsilon_1+(2-p)\varepsilon_{1eff}-2+2p=0 \quad (1)$$

$$(1-p)[\varepsilon_{1eff}\varepsilon_2+\varepsilon_1\varepsilon_{2eff}]-(1+2p)\varepsilon_2+(2-p)\varepsilon_{2eff}=0 \quad (2)$$

where $\varepsilon_{eff}=\varepsilon_{1eff}+i\varepsilon_{2eff}$ and $\varepsilon=\varepsilon_1+i\varepsilon_2$

After some rearrangement of terms, ε_{1eff} and ε_{2eff} can be expressed interm of ε_1 and ε_2 as:

$$\varepsilon_{1eff}=\frac{B}{A} \quad (3)$$

$$\varepsilon_{2eff}=\frac{(1+2p)\varepsilon_2-(1-p)\varepsilon_2\frac{B}{A}}{(1-p)\varepsilon_1+(2-p)} \quad (4)$$

where:

$$A = (1-p)\varepsilon_1 + \frac{(1-p)^2 \varepsilon_2^2}{(1-p)\varepsilon_1 + (2-p)} + (2-p)$$

and

$$B = 2 - 2p + (1+2p)\varepsilon_1 + \frac{(1-p)(1+2p)\varepsilon_2^2}{(1-p)\varepsilon_1 + (2-p)}$$

So, the absorption coefficient (off by a multiplicative factor) of the composite medium consisting of Si dots embedded in an SiO_2 matrix is:

$$\alpha \propto \frac{\varepsilon_{2eff}}{\lambda} = \frac{1}{\lambda} \frac{(1+2p)\varepsilon_2 - (1-p)\varepsilon_2 \frac{B}{A}}{(1-p)\varepsilon_1 + (2-p)}$$

In terms of the refractive index n_{Si}, n_{SiO_2} and extinction coefficient k_{Si}, k_{SiO_2} of Si and SiO_2:

$$\varepsilon(\lambda) = \frac{\varepsilon_{Si}(\lambda)}{\varepsilon_{SiO_2}(\lambda)} = \frac{\varepsilon_{1Si} + i\varepsilon_{2Si}}{\varepsilon_{1SiO_2} + i\varepsilon_{2SiO_2}} = \frac{n_{Si}^2 - k_{Si}^2}{n_{SiO_2}^2} + i\frac{2n_{Si}k_{Si}}{n_{SiO_2}^2} = \varepsilon_1(\lambda) + i\varepsilon_2(\lambda)$$

or

$$\varepsilon_1 = \frac{n_{Si}^2 - k_{Si}^2}{n_{SiO_2}^2} \text{ and } \varepsilon_2 = \frac{2n_{Si}k_{Si}}{n_{SiO_2}^2} \text{ (Note that } \varepsilon_{2SiO_2} = 2n_{SiO_2}k_{SiO_2} = 0)$$

Thus:

$$\alpha \propto \frac{1}{\lambda} \frac{(1+2p)\frac{2n_{Si}k_{Si}}{n_{SiO_2}^2} - (1-p)\frac{2n_{Si}k_{Si}}{n_{SiO_2}^2}\frac{B}{A}}{(1-p)\frac{n_{Si}^2 - k_{Si}^2}{n_{SiO_2}^2} + (2-p)} \qquad (5)$$

With values of the refractive index and extinction coefficients of Si and SiO_2 given in appendix I, the absorption coefficient α for Si dots with a given uniform radius can be obtained by equation [5].

In order to take into account the size distribution of a collection of Si dots with radius r_i and distribution T_i, the average absorption coefficient $\overline{\alpha}$ can be written as:

$$\overline{\alpha} = \sum_i \alpha(r_i) T_i \tag{6}$$

Equation [6] described the absorption coefficient (off by a multiplicative factor) for a composite medium consisting of Si dots with radius r_i and distribution T_i, embedded in an SiO_2 matrix.

References

1 F. Wooten, **Optical Properties of Solids**, Academic Press, New York, 1972.

2 S. S. Iyer and Y. H. Xie, Science **260**, 40 (1993).

3 L. T. Canham, Appl. Phys. Lett. **57**, 1046 (1990).

4 S. M. Prokes, and O. J. Glembocki, Mater. Chem. and Phys. **35**, 1 (1993).

5 S. M. Prokes and W. E. Carlos, Appl. Phys. Lett. **78**, 2671 (1995).

6 S. Schuppler, S. L. Friedman, M. A. Marcus, D. L. Adler, Y. H. Xie, F. M. Ross, Y. J. Chabal, T. D. Harris, L. E. Brus, W. L. Brown, E. E. Chaban, P. F. Szajowski, S. B. Christman, and P. H. Citrin, Phys. Rev. B **52**, 4910 (1995).

7 F. Koch, V. Petrova-Koch, and T. Muschik, J. Lumi. **57**, 271 (1993).

8 J. S. Tse, J. R. Dahn, and F. Buda, J. Phys. Chem. **99**, 1896 (1995).

9 L. Tsybeskov, J. V. Vandyshev, and P. M. Fauchet, Phys. Rev. B **49**, 7821 (1994).

10 M. Yamada, A. Takazawa, and T. Tamura, Jpn. J. Appl. Phys. **31**, L1451 (1992).

11 R. P. Vasquez, R. W. Fathauer, T. George, A. Ksendzow, and T. L. Lin, Appl. Phys. Lett. **60**, 1004 (1992).

12 T. Goerge, M. S. Anderson, W. T. Pike, T. L. Lin, R. W. Fathauer, K. H. Jung, and D. L. Wong, Appl. Phys. Lett. **60**, 2359 (1992).

13 M. S. Brandt, H. D. Fuchs, M. Stutzmann, J. Weber, and M. Cardona, Solid State Comm. **81**, 302 (1992).

14 S. M. Prokes, O. J. Glembocki, V. M. Bermudez, R. Kaplan, L. E. Friedersdorf, and P. C. Searson, Phys. Rev. B **45**, 13788 (1992).

15 K. H. Li, C. Tsai, J. Sarathy, and J. C. Campbell, Appl. Phys. Lett. **62**, 3192 (1993).

16 S. M. Prokes and O. J. Glembocki, Phys. Rev. B **49**, 2238 (1994).

17 A. D. Yoffe, Adv. Phys. **42**, 173 (1993).

18 C. Kittel, **Introduction to Solid State Physics**, John Wiley & Sons, New York, 1976.

19 C. Weisbuch, B. Vinter, **Quantum Semiconductor Structures**, Academic Press, San Diego, California, 1991.

20 R. L. Liboff, **Introductory Quantum Mechanics**, Addison-Wesley Publishing Company, Reading, Massachusetts, 1980.

21 Y. Nosaka, J. Phys. Chem. **95**, 5054 (1991).

22 G. A. Somorjai, **Principles of Surface Chemistry**, Prentice-Hall Inc., EngleWood Cliffs, New York, 1972.

23 L. Brus, Adv. Mat. **5**, 286 (1993).

24 L. C. Feldman, J. W. Mayer, **Fundamentals of Surface and Thin Film Analysis**, North-Holland, New York, 1986.

25 R. J. Hamers, **Scanning Tunneling Microscopy and Spectroscopy-Theory, Techniques, and Applications**, edited by D. A. Bonnell, VCH Publishers, New York,1993, Chap. 4.

26 J. A. Strocio, R. M. Feenstra, **Methods of experimental physics**, edited by Joseph. A. S. and W. J. Kaiser, Academic Press, Boston, 1993, vol. 27, Chap. 4.

27 B. D. Cullity, **X-ray diffraction**, Addison-wesley Publishing Company, Reading, Massachusetts, 1956.

28 S. Wischnitzer, **Introduction to electron microscopy**, Pergamon, New York, 1970.

29 P. Baeri and S. U. Campisano, **Laser Annealing Of Semiconductors**, edited by J. M. Poate and J. W. Mayer, Academic Press, New York, 1982, Chap. 4.

30 R. Kelly, A. Miotello, **Pulsed Laser Deposition of Thin Films**, edited by D. B. Chrisey and G. K. Hubler, John Wiley & Sons, New York, 1994, Chap. 3.

31 A. D. Akhsakhalyan, Yu A. Bityurin, S. V. Gaponov, A. A. Gudkov, and V. I. Luchin, Sov. Phys. Tech. Phys. **27**, 973 (1982).

32 R. Kelly, J. J. Cuomo, P. A. Leary, J. A. Rothenberg, B. E. Braren, and C. F. Aliotta, Nucl. Instrum. Meth. **B9**, 329 (1985).

33 R. Kelly, and J. A. Rothenberg, Nucl. Instrum. Meth. **B7/8**, 755 (1985).

34 K. Kimoto, Y. Kamiya, M. Nonoyama, and R. Uyeda, Jpn. J. Appl. Phys. **2**, 702 (1963).

35 S. Yatsuya, S. Kasukabe, and R. Uyeda, J. Cryst. Growth **24/25**, 319 (1974).

36 H. Haberland, **Clusters of Atoms and Molecules**, Springer-Verlag, Berlin Heidelberg, 1994.

37 Buff F. P., J. Chem. Phys. **19**, 1591 (1951).

38 Mason B. J., **The Physics of Clouds**, Oxford University Press, London, 1971, Chap. 1.

39 Andres R. P., **Nucleation Phenomena**, edited by ...., American Chemical Society, Washington , D. C., p. 17-25.

40 L. Banyai and S. W. Koch, **Semiconductor Quantum Dots**, World Scientific Publishing, Singapore, 1993, p. 215-228.

41 M. Lifshitz and V. V. Slezov, Soviet Phys. JTEP **2**, 331 (1959).

42 S.Kasukabe, J. Cryst. Growth **99**, 196 (1990).

43 J. J. Boland, J. Vac. Sci. Technol. A **10**, 2458 (1992).

44 J. W. Lyding, G. C. Abeln, T. C. Shen, C. Wang, and J. R. Tucker, J. Vac. Sci. Technol. B **12**, 3735 (1994).

45 M. Morita, T. Ohmi, E. Hasegawa, and M. Ohwada, J. Appl. Phys. **68**, 1272 (1990).

46 F. G. Himpsel, F. R. Mcfeely, A. Taleb-Ibrahimi, and J. A. Yarmoff, Phys. Rev. B **38**, 6084 (1988).

47 C. D. Wagner, W. M. Riggs, L. E. Davis, J. F. Moulder, and G. E. Muilenberg, **Handbook of X-ray Photoelectron Spectroscopy**, Perkin-Elmer, Eden Prairie, MN, 1979.

48 M. Morita and T. Ohmi, Jpn J. Appl. Phys. **33**, 370 (1994).

49 H. Nishikawa, T. Shiroyama, R. Nakamura, Y. Ohki, K. Nasagawa, and Y. Hama, Phys. Rev. B **45**, 586 (1992).

50 S. M. Prokes, Appl. Phys. Lett. **62**, 3244 (1993).

51 S. M. Prokes and O. J. Glembocki, Phys. Rev. B **49**, 2238 (1994).

52 See appendix I.

53 R. C. Tatar, S. Rabii, Phys. Rev. B **25**, 4126, 1982.

54 I. R. Collins, P. T. Andrew, and A. R. Law, Phys. Rev. B **38**, 13348 (1988).

55 R. Claessen, H. Carstensen, and M. Skibowski, Phys. Rev. B **38**, 12582 (1988).

56 T. Venkatesen, X. D. Wu, A. Inam, and J. B. Watchman, Appl. Phys. Lett. **52**, 1193 (1988).

57 Due to convolution of the cluster dimensions with the finite radius of the STM tip, STM diameter measurements tended to give values that could be up to 20 % higher than the actual values (i.e., those determined from HRTEM and XRD). On the other hand, STM height measurements of nc-Si on HOPG yielded values that could be up to 200 % lower than actual values. This is because near the Fermi level, where most electrons of the tunneling current come from, a semimetal like graphite usually has a much higher electronic density of states than that of a semiconductor like Si. This causes the tip to approach much closer to the Si nanocrystal than to the graphite substrate for a given tunneling current, and the height of the nanocrystal is therefore underestimated by STM. Height measurements were therefore not used to determine nanocrystal sizes.

58 V. Lehmann, B. Jobst, T. Muschik, A. Kux, and V. Petrova-Koch, Jpn. J. Appl. Phys. **32**, 2095 (1993).

59 V. Petrova-Koch, and Muschik T., Thin Solid Films **255**, 246 (1995).

60 Y. Mochizuki, M. Mizuta, Y. Ochiai, S. Matsui, and N. Ohkubo, Phys. Rev. B **46**, 12353 (1992).

61 N. A. Hill, and K. B. Whaley, Phys. Rev. Lett. **75**, 1130 (1995).

62 L. W. Wang, and A. Zunger, J. Phys. Chem. **98**, 2158 (1994).

63 T. Miyoshi, K. S. Lee, and Y. Aoyagi, Jpn. J. Appl. Phys. **31**, 2470 (1992).

64 L. R. Tessler, F. Alvarez, and O. Teschke, Appl. Phys. Lett. **62**, 2381 (1993).

65 See appendix II

66 Y. Kanemitsu, T. Futagi, T. Matsumoto, and H. Mimura Phys. Rev B **49**, 14732 (1994).

67 C. Delerue, M. Lannoo, and G. Allan, J. Lum. **57**, 249 (1993).

68 L. Banyai and S. W. Koch, **Semiconductor Quantum Dots**, World Scientific Publishing, Singapore, 1993,Chap. 2.

69 G. E. Jellison Jr., Opt. Mat. **1**, 41 (1992).

70 See appendix III, IV

71 See appendix V

72 P. Wickboldt, H. M. Cheong, D. Pang, J. H. Chen, and W. Paul, Mat. Res. Soc. Symp. Proc. **358**, 127 (1995).

73 A. J. Kontkiewicz, A. M. Kontkiewicz, J. Siejka, S. Sen, G. Nowak, A. M. Hoff, P. Sakthivel, K. Ahmed, P. Mukherjee, S. Witanachchi, and J. Lagowski, Appl. Phys. Lett. **65**, 1436 (1994).

74 L. N. Dinh, L. L. Chase, M. Balooch, L. J. Terminello, and F. Wooten, Appl. Phys. Lett. **65**, 3111 (1994).

75 L. N. Dinh, M. Balooch, and L. L. Chase (unpublished).

76 L. N. Skuja, A. N. Streletsky, and A. B. Pakovich, Solid State Communications **50**, 1069 (1984).

77 J. H. Stathis, and M. A. Kastner, Phys. Rev. B **35**, 2972, (1987).

78 A. Kux, D. Kovalev, and F. Koch, Thin Solid Films **255**, 143 (1995).

79 I. A. Movtchan, R. W. Dreyfus, W. Marine, M. Sentis, M. Autric, G. Lelay, N. Merk, Thin Solid Films **255**, 286 (1995).

80 In XAS, the wavelength (or energy) of the incident x-ray is scanned around some absorption edge of the sample under study. Here, the absorption edge refers to the photon energy needed to promote an electron from a core level to the Fermi level for a metal, or to the bottom of the conduction band for a semiconductor. The photo-induced current measured from the sample is directly proportional to the absorption intensity.

81 The AFM records the interatomic force between the apex of a tip and atoms in a sample as the tip is scanned over the surface of the sample. When the AFM is operated in a mode that senses the repulsive forces between tip and sample, the tip actually touches the sample , much like the case of a stylus in a record player. For the AFM, however, the tip is much sharper and the tracking force is much smaller. The AFM can also be operated so that it senses the attractive forces between tip and sample. The feedback system then prevents the tip from touching and damaging the sample. The small repulsive forces between the tip and the sample , usually in the range of 10^{-6} to 10^{-9} N, are recorded by measuring minute deflections of the cantilever (a small tip attached to a spring). If a deflection as small as 1 nm can be sensed for a cantilever with a spring constant of 1N/m, then a tracking force as low as 10^{-9} N can be applied between the tip and the sample. Microcantilever made of silicon oxide with silicon etching technology are very light and have resonant frequencies as high as 100-400 kHz. The higher the resonnant frequency, the less sensitive the cantilever is

to vibrations in the environment, and the more stable it is for atomic force microscopy. Thus, with some additional vibration isolation, such a cantilever would be suitable for atomic force microscopy. The deflection of the spring can be measured by an interferometer or simply by the deflection of a laser beam reflected off the back of the tip. A feedback circuit controls the voltage applied to a z piezo element so that the signal is held constant as the tip is scanned across the surface of the sample with the x piezo. So, the AFM has an excellent resolution in the vertical direction, and in this experiment, cluster size measured by AFM refers to AFM height measurement.

82 W. Eberhardt, G. Kalkoffen, C. Kunz, D. Aspnes and M. Cardona, Phys. Stat. Sol. **88**, 135 (1978).

83 T. VanBuuren, Ph.D. thesis, University of British Columbia, 1995.

84 Y. Kanemitsu, T. Ogawa, K. Shiraishi, and K. Takeda, Phys. Rev. B **48**, 4883 (1993).

85 R. Williams, Phys. Rev. **140**, A569 (1965).

86 S. I. Fedoseenko, V. K. Adamchuk and V. V. Afana'ev, Microelectron. Eng. **22**, 367 (1993).

87 L. N. Skuja and A. R. Silin, Phys. Status Solidi A **56**, K11 (1979).

88 K. Nagasawa, Y. Ohki, and Y. Hama, Jpn. J. Appl. Phys. **26**, L1009 (1987).

89 S. Munekuni, T. Yamanaka, Y. Shimogaichi, R. Tohmon, Y. Ohki, K. Nagasawa, and Y. Hama, J. Appl. Phys. **68**, 1212 (1990).

90 K. Nagasawa, Y. Hoshi, Y. Ohki, and K. Yahagi, Jpn. J. Appl. Phys. **25**, 464 (1986).

91 A. F. Jones and D. L. Misell, Brit. J. Appl. Phys. **18**, 1479 (1967).

92 **Nanospec/AFT (Automated Film Thickness Measurement System)**, Nanometrics Incorporated, Sunnyvale, CA, 1993.

93 A. Sommerfeld, **Elektrodynamik**, Akademische Verlagsgesellschaft Geest & Portig K. G., Leipzig, 1949.

94 C. F. Bottcher, **Theory of Electric Polarization**, Elsevier, Amsterdam, 1973.